Non-linear magnetohydrodynamic modeling of plasma response to resonant magnetic perturbations

F. Orain, M. Bécoulet, G. Dif-Pradalier, G. Huijsmans, S. Pamela, E. Nardon, C. Passeron, G. Latu, V. Grandgirard, A. Fil, A. Ratnani, I. Chapman, A. Kirk, A. Thornton, M. Hoelzl, and P. Cahyna

Citation: Physics of Plasmas (1994-present) **20**, 102510 (2013); doi: 10.1063/1.4824820
View online: http://dx.doi.org/10.1063/1.4824820
View Table of Contents: http://scitation.aip.org/content/aip/journal/pop/20/10?ver=pdfcov
Published by the AIP Publishing

Non-linear magnetohydrodynamic modeling of plasma response to resonant magnetic perturbations

F. Orain,[1] M. Bécoulet,[1] G. Dif-Pradalier,[1] G. Huijsmans,[2] S. Pamela,[3] E. Nardon,[1] C. Passeron,[1] G. Latu,[1] V. Grandgirard,[1] A. Fil,[1] A. Ratnani,[1] I. Chapman,[4] A. Kirk,[4] A. Thornton,[4] M. Hoelzl,[5] and P. Cahyna[6]
[1]*CEA, IRFM, F-13108 Saint-Paul-Lez-Durance, France*
[2]*ITER Organization, Route de Vinon, F-13115 Saint-Paul-Lez-Durance, France*
[3]*IIFS-PIIM. Aix Marseille Université - CNRS, 13397 Marseille Cedex20, France*
[4]*EURATOM/CCFE Fusion Association, Culham Science Centre, Oxon OX14 3DB, United Kingdom*
[5]*Max-Planck-Institut für Plasmaphysik, EURATOM Association, Garching, Germany*
[6]*Association EURATOM/IPP.CR, Prague, Czech Republic*

(Received 3 July 2013; accepted 26 September 2013; published online 16 October 2013)

The interaction of static Resonant Magnetic Perturbations (RMPs) with the plasma flows is modeled in toroidal geometry, using the non-linear resistive MHD code JOREK, which includes the X-point and the scrape-off-layer. Two-fluid diamagnetic effects, the neoclassical poloidal friction and a source of toroidal rotation are introduced in the model to describe realistic plasma flows. RMP penetration is studied taking self-consistently into account the effects of these flows and the radial electric field evolution. JET-like, MAST, and ITER parameters are used in modeling. For JET-like parameters, three regimes of plasma response are found depending on the plasma resistivity and the diamagnetic rotation: at high resistivity and slow rotation, the islands generated by the RMPs at the edge resonant surfaces rotate in the ion diamagnetic direction and their size oscillates. At faster rotation, the generated islands are static and are more screened by the plasma. An intermediate regime with static islands which slightly oscillate is found at lower resistivity. In ITER simulations, the RMPs generate static islands, which forms an ergodic layer at the very edge ($\psi \geq 0.96$) characterized by lobe structures near the X-point and results in a small strike point splitting on the divertor targets. In MAST Double Null Divertor geometry, lobes are also found near the X-point and the 3D-deformation of the density and temperature profiles is observed.
 [http://dx.doi.org/10.1063/1.4824820]

I. INTRODUCTION

The Edge Localized Modes (ELMs) are peeling-ballooning instabilities which develop in H-mode tokamak plasmas. They are characterized by the release of quasi-periodical bursts of energy and particles through the external transport barrier. The large type-I ELMs would represent a particular concern for the ITER divertor if they were not controlled,[1] and the application of external Resonant Magnetic Perturbations (RMPs) is one of the most promising method to control them. Indeed, the total suppression of the type-I ELMs by RMPs was demonstrated in DIII-D[2,3] and later in ASDEX upgrade[4] and KSTAR;[5] the strong mitigation of the ELM size was also obtained in the JET,[6] MAST,[7] and NSTX[8] tokamaks, motivating the use of this method in ITER.[2,9] The non-linear MHD theory and modeling made significant progress to refine the understanding of the RMP interaction with the plasma.[10–15] In particular, it was demonstrated that the penetration of the RMPs in the plasma is conditioned by the rotating plasma response.[11–15] The generation of current perturbations on the rational surfaces in the plasma can prevent magnetic reconnection, leading to the screening of RMPs. However, at certain plasma parameters, RMPs can on the contrary be amplified.[16] Non-linear MHD modeling of the rotating plasma response to RMPs in cylindrical geometry[11,12] demonstrated that the poloidal plasma rotation, including the $\vec{E} \times \vec{B}$ and diamagnetic rotations, both perpendicular to the magnetic field, are particularly important in the pedestal region and are likely to screen the RMPs. The aim of the present work is to extend the previous RMP modeling[12] to the more realistic toroidal geometry of the tokamak, including the X-point and the Scrape-Off Layer (SOL). The reduced MHD code JOREK[17] was enhanced to take into account the physics of the flows and the RMPs and then used for simulations. The physical model used is described in Sec. II. In Secs. III–V, the penetration of the RMPs in the rotating plasma is studied in JET-like, ITER, and MAST geometries, respectively. In Sec. III, the JET plasma flows in the SOL and the pedestal are first described without RMPs. Three regimes of plasma response to RMPs are highlighted which depend on the plasma resistivity and on diamagnetic rotation. The screening of the RMPs on the resonant surfaces is also discussed. In Sec. IV, the ergodization of the very edge is observed in ITER with RMPs; lobe structures near the X-point and 3D-corrugation are described. The screening effect of the plasma rotation on the lobe size is demonstrated. In the Double-Null MAST geometry, the edge is also shown to be ergodized by the RMPs in Sec. V, going along with the 3D-deformation of the density and temperature profiles. Last, conclusions are given in Sec. VI.

II. PHYSICAL MODEL

The plasma response to RMPs is studied with the nonlinear reduced MHD code JOREK[17] in toroidal geometry including the X-point and the SOL. The four-field model,[17,18] which encompasses the continuity equation, the parallel and perpendicular projections of the momentum equation, the energy equation and Ohm's law, is used as basic set of equations. Compared to Ref. 17, two-fluid diamagnetic effects, neoclassical friction and a source of toroidal rotation corresponding to the experimental profile are introduced in the model so as to self-consistently study the interaction between plasma flows and RMPs.

The magnetic field is decomposed in toroidal and poloidal components: $\vec{B} = F_0 \nabla\varphi + \nabla\psi \times \nabla\varphi$, where φ is the toroidal angle, ψ is the poloidal flux, and $F_0 = R_0 B_{\varphi 0}$; R_0 is the major radius and $B_{\varphi 0}$ is the toroidal magnetic field amplitude at the magnetic axis. In the framework of the reduced MHD, F_0 is supposed to be constant in time, and the poloidal magnetic field is assumed to be much lower than the toroidal one.

The two-fluid diamagnetic effects are added to the initial model:[17] the diamagnetic velocity $\vec{V}_s^* = -\nabla P_s \times \vec{B}/(\rho e_s B^2/m_i)$ is taken into account for each species s (electrons and ions) and is of special importance in the pedestal where the pressure profile is steep. P_s is the scalar pressure of the species s, e_s is the charge of the species, m_i is the ion mass, and $\rho = m_i \times n$ is the ion mass density, where $n = n_e = n_i$ is the particle density. The decomposition of the fluid velocity then writes

$$\vec{V} \approx \vec{V}_i = \vec{V}_{||,i} + \vec{V}_E + \vec{V}_i^*, \tag{1}$$

where $\vec{V}_E = \vec{E} \times \vec{B}/B^2$ is the electric drift velocity.

As for the neoclassical effects, they are considered in the momentum equation, where the pressure tensor is written as $\bar{P} = \bar{I}P + \bar{\Pi}_{i,neo} + \bar{\Pi}_{i,gv}$. The cancellation of the gyroviscous tensor $\nabla \cdot \bar{\Pi}_{i,gv}$ with the time derivative of the diamagnetic velocity $d\vec{V}_i^*/dt$ is used,[19] and the divergence of the neoclassical tensor is given by the heuristic closure taken from Ref. 20

$$\nabla \cdot \bar{\Pi}_{i,neo} = \rho \mu_{i,neo} \frac{B^2}{B_\theta^2} (V_\theta - V_{\theta,neo}) \vec{e}_\theta, \tag{2}$$

where $\mu_{i,neo}$ is the neoclassical friction. This formulation expresses the friction between trapped and passing particles and constrains the poloidal velocity V_θ to approach the neoclassical value $V_{\theta,neo} = -k_i \nabla T_i \times \vec{B}/eB^2 \cdot \vec{e}_\theta$, where k_i is the neoclassical heat diffusivity. We have used the following definition of the unit vector in the poloidal direction:

$$\vec{e}_\theta = (\nabla\psi \times \nabla\varphi) \frac{R}{|\nabla\psi|}. \tag{3}$$

Note that this definition implies that the orthonormal basis $(\vec{e}_\psi, \vec{e}_\theta, \vec{e}_\varphi) = (\frac{\nabla\psi}{|\nabla\psi|}, (\nabla\psi \times \nabla\varphi)\frac{R}{|\nabla\psi|}, R\nabla\varphi)$ is left handed, and the poloidal magnetic field therefore writes

$$B_\theta = B \cdot \vec{e}_\theta = |\nabla\psi|/R. \tag{4}$$

In JOREK, the grid is discretized in 2D bi-cubic Bézier finite elements in the poloidal plane, and the toroidal direction is decomposed in Fourier series.[17] Each Bézier element has its local coordinates (s,t), and the local system (s,t,φ) is related to the global cylindrical (R,Z,φ) coordinate system in which the equations are defined, using the co- and contravariant vectors. In this paper, the intrinsic flux aligned coordinate system $(\nabla\psi_0, \nabla\theta, \nabla\varphi)$, more convenient for physical understanding, is also used. The equilibrium flux surfaces (defined by the equilibrium poloidal flux ψ_0) are calculated by solving the Grad-Shafranov equation and the intrinsic poloidal angle θ is obtained from the equation: $d\theta/d\varphi = -1/q$ where q is the safety factor.

The following system of Eqs. (5)–(9) is solved for the mass density ρ, the parallel (ion) velocity $V_{||,i}$, the perpendicular velocity $V_\perp$, the temperature T, and the magnetic flux ψ, normalized in JOREK units (the normalizations are described below):

$$\frac{\partial\rho}{\partial t} = -\nabla(\rho\vec{V}) + \nabla \cdot (D_\perp \nabla_\perp \rho) + S_\rho, \tag{5}$$

$$\rho \frac{F_0}{R} \frac{\partial V_{||,i}}{\partial t} = \vec{b} \cdot (-\rho(\vec{V} \cdot \nabla)(\vec{V}_{||,i} + \vec{V}_E)) - \nabla P - \bar{\nabla} \cdot \bar{\Pi}_{i,neo}) + \mu_{||} \Delta V_{||,i} + S_{v_{||}}, \tag{6}$$

$$\vec{e}_\varphi \cdot \nabla \times \left(\rho \frac{\partial \vec{V}_E}{\partial t} = -\rho(\vec{V} \cdot \nabla)(\vec{V}_{||,i} + \vec{V}_E) + \vec{J} \times \vec{B} - \nabla P - \bar{\nabla} \cdot \bar{\Pi}_{i,neo} + \mu_\perp \Delta V \right), \tag{7}$$

$$\rho \frac{\partial T}{\partial t} = -\rho\vec{V} \cdot \nabla T - (\gamma - 1) P \nabla \cdot \vec{V} + \frac{1}{2} V^2 S_\rho + \nabla \cdot (\kappa_{||} \nabla_{||} T + \kappa_\perp \nabla_\perp T) + (1 - \gamma) S_T, \tag{8}$$

$$\frac{1}{R^2} \frac{\partial\psi}{\partial t} = -\vec{B} \cdot \nabla_{||} u + \frac{\tau_{IC}}{\rho} \vec{B} \cdot \nabla_{||} P + \frac{\eta J}{R^2}, \tag{9}$$

where the parallel gradient is defined as

$$\nabla_{||}\alpha = (\vec{B}/B^2)\vec{B} \cdot \nabla\alpha = \frac{\vec{b}}{B} \left(\frac{F_0}{R^2} \partial_\varphi \alpha + \nabla\varphi \cdot \nabla\alpha \times \nabla\psi \right). \tag{10}$$

The normalization of the variables in JOREK units (noted with superscript $\sim$) is the following: time is defined as $t = \tilde{t}\sqrt{\rho_0\mu_0}$, mass density is $\rho = \tilde{\rho}\rho_0$, temperature is $T(eV) = m_i/(\rho_0\mu_0 e)\tilde{T}$, the total pressure is $\tilde{P} = \mu_0 P = \tilde{\rho}\tilde{T}$, and the toroidal current is $\tilde{J} = \mu_0 J$. Note that the toroidal current density is defined as $j = \Delta_\perp \psi = -R^2 \vec{J} \cdot \nabla\varphi$ and hence in JOREK system a co-current injection corresponds to a negative source of parallel velocity. The electrostatic potential $\tilde{u}$ is related to the electric field as $\vec{E} = -F_0 \nabla\tilde{u}/\sqrt{\rho_0\mu_0}$. For each species s, the parallel and perpendicular components of the velocity are $\vec{V}_{||,s} = \tilde{V}_{||,s}\vec{B}/\sqrt{\rho_0\mu_0}$ ($\tilde{V}_{||,s}$ has no dimension) and $V_{\perp,s} = \tilde{V}_{\perp,s}/\sqrt{\rho_0\mu_0}$ ($\tilde{V}_{\perp,s}$ is expressed in Tesla). Once normalized, the decomposition of the fluid (ion) velocity (1) therefore becomes

$$\vec{V} = V_{||,i}\vec{B} - R^2 \nabla u \times \nabla\varphi - \frac{R^2 \tau_{IC}}{\rho} \nabla P \times \nabla\varphi, \tag{11}$$

where the inverse of the normalized ion cyclotron frequency is defined as $\tau_{IC} = m_i/(2F_0 e\sqrt{\rho_0\mu_0})$. The electron and ion temperatures T_e and T_i are assumed to be equal in the model used here.

The projection of Eq. (11) along the poloidal direction $\vec{e}_\theta$ (3) gives the expression of the poloidal velocity

$$V_\theta = -\frac{1}{B_\theta}\left(\nabla_\perp\psi\cdot\nabla_\perp u + \frac{\tau_{IC}}{\rho}\nabla_\perp\psi\cdot\nabla_\perp P - V_{||,i}B_\theta^2\right). \tag{12}$$

The combination of Eqs. (12) and (3) with the expression of the normalized neoclassical velocity $V_{\theta,neo} = -\frac{k_i\tau_{IC}}{B_\theta}\times(\nabla_\perp\psi\cdot\nabla_\perp T)$ leads to the developed form of the neoclassical tensor (2)

$$\nabla\cdot\bar{\Pi}_{i,neo} = \mu_{i,neo}\rho\frac{B^2}{B_\theta^4}\left(-V_{||,i}B_\theta^2 + \nabla_\perp\psi\cdot\nabla_\perp u + \frac{\tau_{IC}}{\rho}(\nabla_\perp\psi\cdot\nabla_\perp P + k_i\rho\nabla_\perp\psi\cdot\nabla_\perp T)\right)(\nabla\psi\times\nabla\varphi). \tag{13}$$

Realistic radial profiles of the neoclassical parameters $\mu_{i,neo}$ and k_i (calculated from Ref. 21), which depend both on the aspect ratio and on the collisionality, are used in the simulations for the JET case (Sec. III). For the sake of simplicity, these coefficients are taken constant in the ITER case (Sec. IV), where typical values $\tilde{\mu}_{i,neo} = \mu_{i,neo}\sqrt{\rho_0\mu_0} = 10^{-5}$ and $k_i = -1$ (Ref. 12) are used. In the MAST case, the neoclassical friction is not included in the model.

$D_\perp$ is the perpendicular particle diffusion, $\mu_{||}$ and $\mu_\perp$ are the parallel and perpendicular anomalous viscosity coefficients, $\gamma = 5/3$ is the adiabatic index, $\kappa_{||}$ and $\kappa_\perp$ are the parallel and perpendicular heat diffusivity, and η is the resistivity. These parameters are normalized as $\tilde{D}_\perp = D_\perp\sqrt{\rho_0\mu_0}$, $\tilde{\kappa}_{(||,\perp)} = \kappa_{(||,\perp)}\sqrt{\rho_0\mu_0}$, $\tilde{\mu}_{(||,\perp)} = \mu_{(||,\perp)}\sqrt{\mu_0/\rho_0}$ and $\tilde{\eta} = \eta\sqrt{\rho_0/\mu_0}$. Both viscosity and resistivity follow a Spitzer-like $(T/T_0)^{-3/2}$ dependence and the parallel heat diffusivity varies as $(T/T_0)^{5/2}$. In the core plasma, for a particle density $n_0 = 6\times10^{19}\mathrm{m}^{-3}$ (JET case), the typical values used in simulations are $D_\perp = \kappa_\perp = 2\mathrm{m}^2/\mathrm{s}$, $\kappa_{||}/\kappa_\perp = 2\times10^8$, $\mu_\perp = 4\times10^{-7}\mathrm{kg/(ms)}$, $\mu_{||}/\mu_\perp = 10$ and $\eta\sim10^{-7}\Omega\cdot\mathrm{m}$.

S_ρ, $S_{V_{||}}$, and S_T are sources of particles, parallel momentum, and heat, respectively. The source of parallel rotation $\tilde{S}_{v_{||}} = -\tilde{\mu}_{||}\Delta\tilde{V}_{||,t=0}$ forces the parallel velocity close to the experimental rotation profile and compensates the losses due to the parallel viscosity. Reproducing realistic sources of heat and particle is a difficult issue.[22] We have opted here for a simple approach: the particle source is constant throughout the plasma, and the radial profile of the heat source is everywhere proportional to the temperature profile.

At the boundary of the computational domain, Dirichlet conditions are used for all the variables, except for the parallel velocity, temperature, and density on the divertor targets. There, Bohm conditions are set (the parallel velocity is equal to the sound speed C_s) and the temperature and density outflow are left free. Consequently, the parallel and perpendicular flows self-consistently evolve towards an equilibrium both in the bulk plasma and the SOL, since they are constrained by Bohm conditions, neoclassical and diamagnetic effects, and the source of parallel rotation. This results in the self-consistent evolution of the radial electric field, expressed by the radial force balance (in JOREK units)

$$E_r = \frac{\tau_{IC}}{\rho}\frac{\nabla_\perp\psi\cdot\nabla_\perp P}{|\nabla\psi|} + \frac{1}{F_0}(V_\theta B_\varphi - B_\theta V_\varphi). \tag{14}$$

The equilibrium flows are established in a time scale of $\sim10^3$ Alfven times t_A. Once they are obtained, perturbation modes ($n\neq0$) including the perturbation due to RMPs are added to the simulation. In the simulations described below, only the fundamental mode $n=0$ and the toroidal harmonic corresponding to the symmetry of the Error Field Correction Coil (EFCC) ($n=2$ in JET) or the RMP coils ($n=3$ in ITER and MAST) are included. The interaction of the "RMP-mode" with unstable modes (ELMs) will be studied in a future work. The application of the RMPs is modeled by a change in boundary conditions for the magnetic flux perturbation. The vacuum RMP spectrum is previously calculated with the ERGOS code[23] and applied as boundary conditions of the computational domain for the magnetic flux perturbation. RMPs are progressively switched on in time: the amplitude of the perturbation is gradually increased in the typical timescale $t\sim1000t_A$. That way, the magnetic perturbation gradually penetrates inside the plasma, which self-consistently adapts in the process. Also this method avoids possible problems with hysteresis effects that could occur if the simulation was started with a fully penetrated magnetic perturbation:[24] the bifurcation from a fully penetrated state to a partially penetrated state might lead to a different plasma response. Note that this approach does not enable the plasma to modify the magnetic field perturbation at the boundary of the computational domain. Yet as this boundary is located far from the confined plasma (in the far SOL or at the wall), the vacuum approximation at the boundary may not be too far from reality. A more correct way to proceed is to include the real field generated by the RMP coils in a free boundary domain. This is under implementation and should be used in future works.

III. JET-LIKE STUDY

A. Input parameters

In this section, JOREK is initialized with JET-like plasma parameters: $R = 3\,\mathrm{m}, a = 1\mathrm{m}, B_t = 2.9\mathrm{T}, q_{95}\sim3$ in toroidal geometry including the X-point. Typical H-mode density and temperature profiles are chosen: the central electron density is $n_{e,0} = 6\times10^{19}\mathrm{m}^{-3}$, the central temperature is $T_{e,0} = 5$ keV, and the central toroidal rotation is $\Omega\sim9$ kHz. Input profiles are given in Fig. 1. Realistic profiles of the neoclassical coefficients are used in this section, given in Fig. 2. The RMP spectrum generated by the external EFCCs is considered in the simulations, with the following configuration: a toroidal symmetry $n=2$ is taken and a current $I_{coil} = 40kAt$ is injected in the EFCC. The vacuum magnetic flux perturbation calculated with ERGOS is given in Fig. 3.

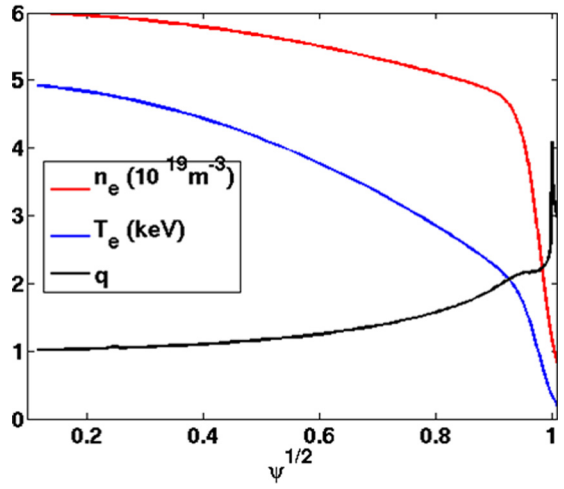

FIG. 1. Initial radial profiles at $t=0$ for JET-like simulations: electron temperature T_e in keV, density n_e in $10^{19}\mathrm{m}^{-3}$, and safety factor q. These profiles are typical experimental JET profiles (previously used in simulations in Ref. 17); the q-profile is almost flat in the pedestal due to the bootstrap current.

B. Equilibrium plasma flows

The modeling of the plasma flows in a consistent way is primordial since they impact the penetration or the screening of the RMPs. In this subsection, equilibrium plasma flows are first studied without RMPs, in order to highlight the patterns generated by the different effects both in the scrape-off layer and the pedestal, in the poloidal and toroidal directions.

In the SOL, the poloidal and toroidal flows are mainly set by the sheath boundary conditions: the parallel $Mach=1$ condition ($V_{||}=\pm C_s$, where C_s is the ion sound speed) set on the divertor targets results in the evolution of the parallel velocity in the SOL until an equilibrium parallel flow is reached, characterized by an opposite direction in the low and high field sides and a bounce point located at the top of the SOL (Fig. 4). The divergence-free condition of the velocity thus constrains also the poloidal flow pattern (Fig. 5) in the SOL.

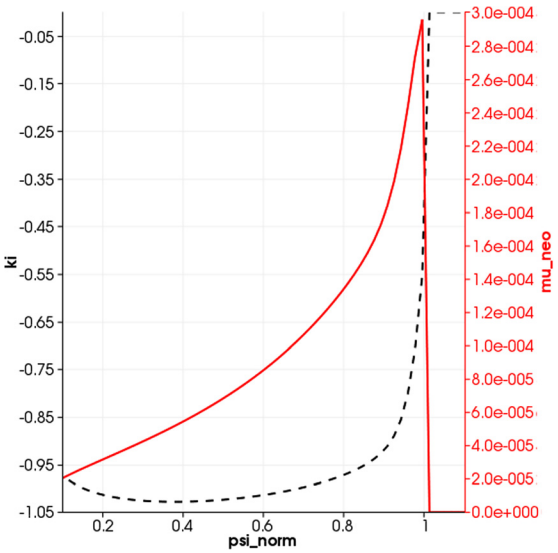

FIG. 2. Realistic radial profiles of the neoclassical coefficients k_i (left axis) and $\mu_{i,neo}$ (right axis) used for simulations in the JET case.

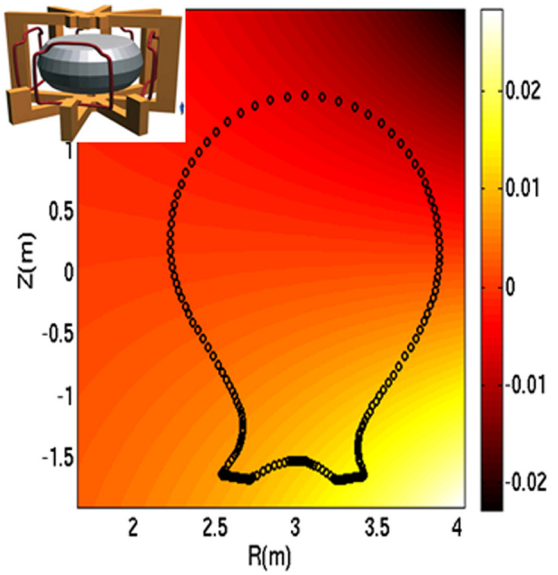

FIG. 3. Cosine component of the $n=2$ magnetic flux perturbation generated by EFCC for $I_{coil}=40kAt$. The black dots correspond to the boundary of the computational domain where the perturbations are applied.

As for the central plasma, the parallel velocity (Fig. 4) is constrained by the source of parallel velocity which mimics the experimental profiles. In the poloidal direction, the flows (Fig. 5) are close to their neoclassical prediction (Fig. 6), especially in the strong temperature gradient pedestal region where neoclassical damping is strong.

The radial electric field E_r (Fig. 7) resulting from the equilibrium force balance (14) adapts accordingly. In particular, in the pedestal, a deep electric field well is generated by the diamagnetic terms (Fig. 7), reaching up to $-10^5\mathrm{V/m}$, which is in the ballpark of the values measured in the experiments.[25] The E_r well obtained in our simulations is five times deeper than in the pulse considered in Ref. 25, but this is consistent with the fact that the pedestal is much higher in our case and thus diamagnetic effects are larger. Indeed, the values of the density ($5\times10^{19}\mathrm{m}^{-3}$) and temperature (2 keV)

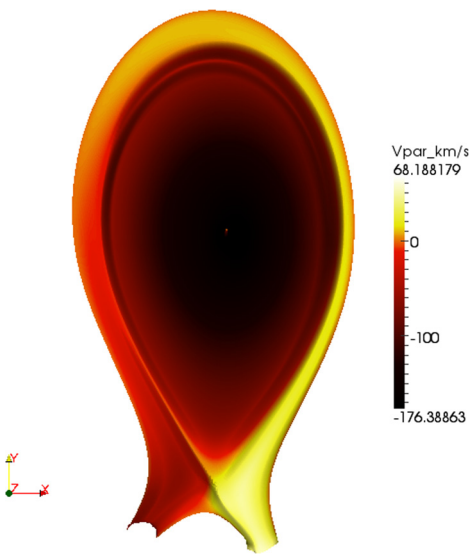

FIG. 4. Parallel velocity (in km/s) in the JET case.

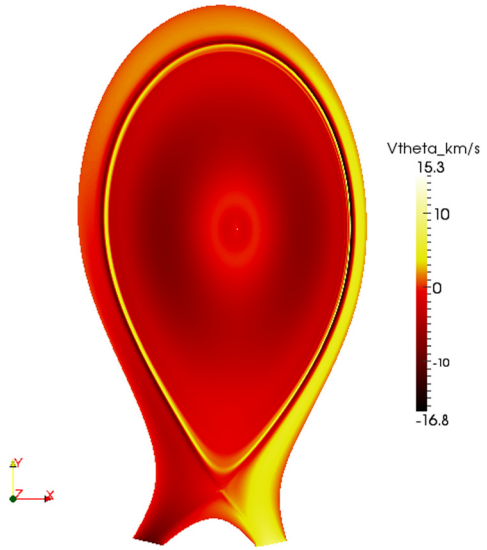

FIG. 5. Poloidal velocity (in km/s) in JET.

at the top of the pedestal are 2–3 times larger in the simulation than in the experimental pulse.[25] We can also note in Fig. 7 that the toroidal source of rotation ($f_{tor} = 9\,\text{kHz}$) combined with the neoclassical effects make the radial electric field positive in the core. Indeed, in the core plasma, the pressure gradient is close to zero and the poloidal velocity is close to the neoclassical value (proportional to the low temperature gradient), so the radial electric field approximates $E_r = -B_\theta V_\varphi$ in order to satisfy the radial force balance (14). The radial electric field is thus positive in the core and negative in the pedestal, so the perpendicular electron velocity $V_{\perp,e} = V_{E\times B} + V_e^*$ (depending on E_r) is zero on a particular surface at the top of the pedestal. If this surface is a rational surface ($q = m/n$, n being the mode driven by the RMPs), the magnetic perturbation is likely to fully penetrate.[11,12,26] The radial profiles of the parallel, poloidal, neoclassical and perpendicular velocities, and the radial electric field are given in Fig. 8 (Low Field Side, LFS) and Fig. 9 (High Field Side) at the midplane.

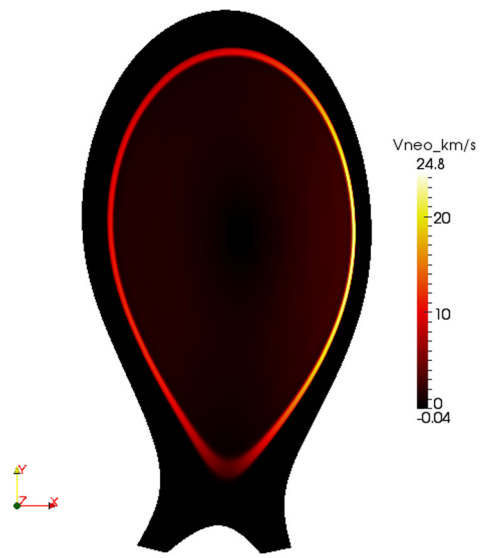

FIG. 6. Neoclassical velocity (in km/s) in JET.

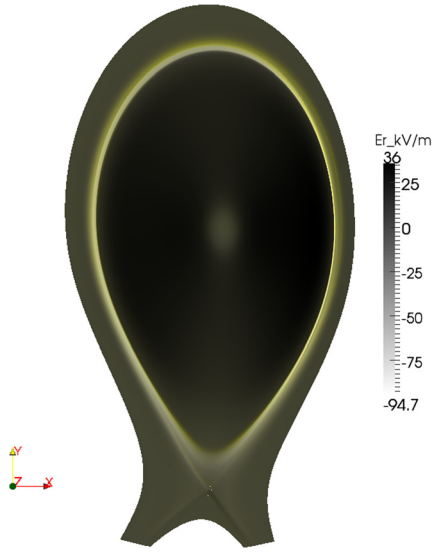

FIG. 7. Radial electric field (in kV/m) in JET with diamagnetic effects, neoclassical effects, and the source of toroidal rotation.

C. RMP screening by large diamagnetic rotation and low resistivity

Once equilibrium flows are established, RMPs ($n = 2$, generated by EFCC, $I_{coil} = 40kAt$) are progressively increased at the boundary in $\sim 1000 t_A$. Without RMPs, the mode $n = 2$ is marginally stable (Fig. 10). In the presence of RMPs, the flux of magnetic perturbation (Fig. 11) penetrates inside the plasma: the energy of the $n = 2$ toroidal mode grows, until a quasi-steady state is reached (Fig. 10). On the resonant surfaces ($q = m/n, n = 2, m \geq 3$), magnetic islands grow up to the saturation, due to reconnection forced by magnetic perturbations. Parallel current perturbations (Fig. 12) are induced on these resonant surfaces in response to the magnetic perturbations and allow for the screening of the RMPs: if the response current is in phase with the radial magnetic perturbation on a given resonant surface, the corresponding RMP harmonic is screened. If the magnetic and current perturbations are in antiphase, the magnetic perturbation penetrates on the corresponding resonant surface as in vacuum and can even be amplified.[12]

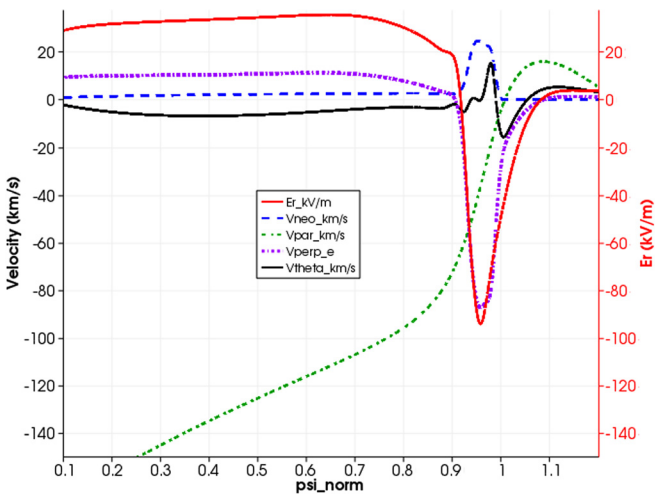

FIG. 8. Radial profiles of the parallel, poloidal, and neoclassical velocities and radial electric field at the low field side at the midplane.

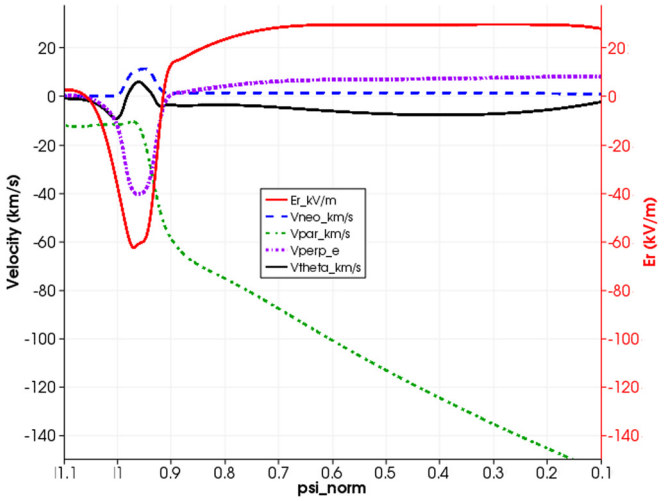

FIG. 9. Radial profiles of the parallel, poloidal, and neoclassical velocities and radial electric field at the high field side at the midplane.

These induced currents depend both on the plasma flows and on the resistivity, so the different terms influencing the flows (diamagnetic velocity, neoclassical friction, and source of parallel rotation) and affecting the plasma response to RMPs are progressively added in the simulation. The central resistivity is scanned between $\eta_0 = 10^{-7}$ and $\eta_0 = 5 \times 10^{-8}$ (in JOREK units). Note that for numerical reasons these values are taken $1-2$ orders of magnitude larger than the realistic (Spitzer) value in JET ($\sim 10^{-9}$).

The effects of the diamagnetic flow and the resistivity are first studied; the source of parallel momentum and then the neoclassical friction are added in the model over a second phase. In all the studied cases, the central harmonic of the perturbation located on the resonant surfaces $q = 3/2$ is screened. The Poincaré plot of the magnetic topology is given in Fig. 13 (here for low poloidal rotation $\tau_{IC} = 10^{-3}$ and high resistivity $\eta_0 = 10^{-7}$). Note that θ_{geom} (only used in the Poincaré plots) represents the geometric poloidal angle, which differs from the intrinsic angle θ defined in Sec. II. θ_{geom} is defined as follows:

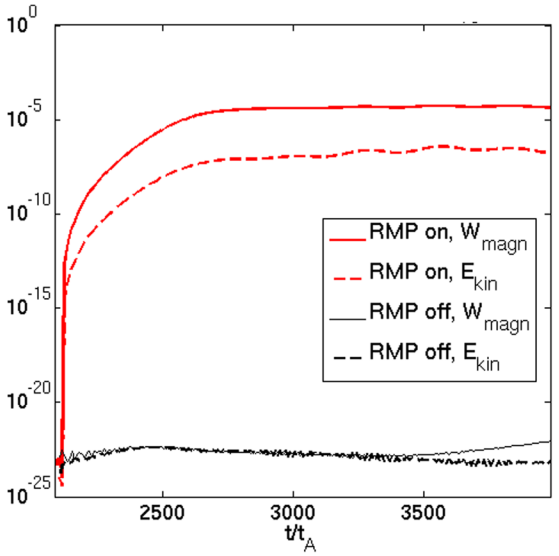

FIG. 10. Magnetic and kinetic energy of the mode $n=2$ without/with RMPs, at high resistivity $\eta_0 = 10^{-7}$ and slow diamagnetic rotation ($\tau_{IC} = 10^{-3}$).

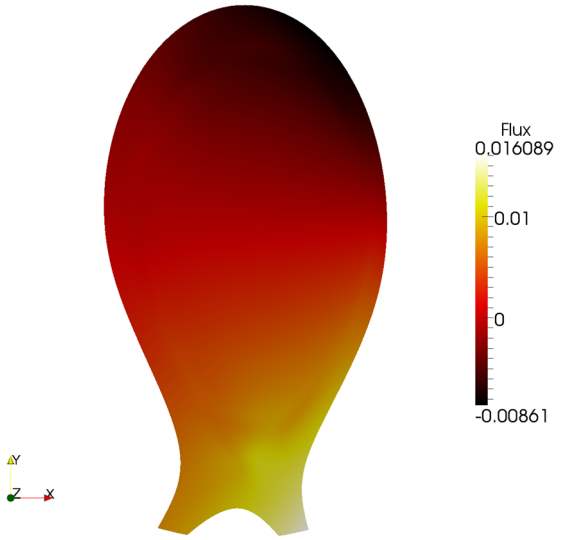

FIG. 11. $n=2$ magnetic flux perturbation $\psi_{n=2}$ penetrating in the plasma ($\eta_0 = 10^{-7}$, $\tau_{IC} = 10^{-3}$).

$$\theta_{geom} = \begin{cases} \arctan((Z-Z_0)/(R-R_0)) & \text{for } R > R_0 \\ \left(\pi - \arctan\left|\dfrac{Z-Z_0}{R-R_0}\right|\right) \times \text{sign}(Z-Z_0) & \text{otherwise.} \end{cases}$$

The Poincaré plot (Fig. 13) shows that small islands are generated on the resonant surface $q = 4/2$: this means that the screening of the $(m = 4, n = 2)$ harmonic is only partial. However, the magnetic perturbation mostly penetrates at the very edge of the plasma where the resistivity is higher (Fig. 13). In these simulations, the magnetic shear is strong for $q \geq 2.5$ (Fig. 1) so the proximity of the surfaces $q = 5/2$ and $q = 6/2$ explains the formation of a stochastic layer at the edge, for $\psi \geq 0.97$ (Fig. 13). Yet, since the modes $m \geq 6$ are located too close to the separatrix, only the mode $m = 5$ seems to develop significantly, as suggests the structure of the density and temperature perturbations presented in Figs. 14 and 15. It is also interesting to note that the coupling of

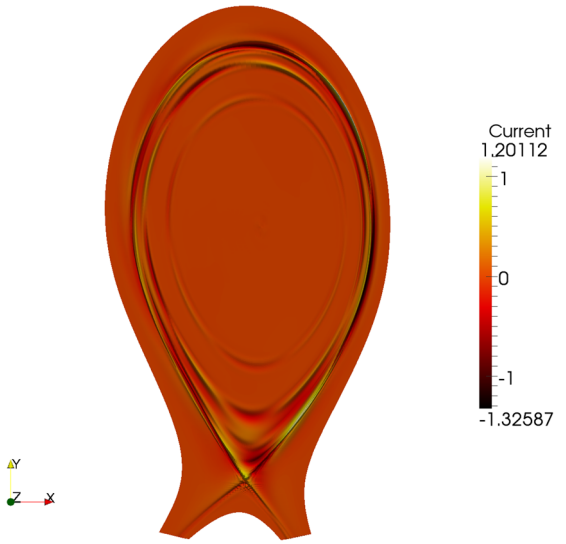

FIG. 12. Response toroidal current perturbation $J_{n=2}$ on the resonant surfaces due to RMPs ($\eta_0 = 10^{-7}$, $\tau_{IC} = 10^{-3}$).

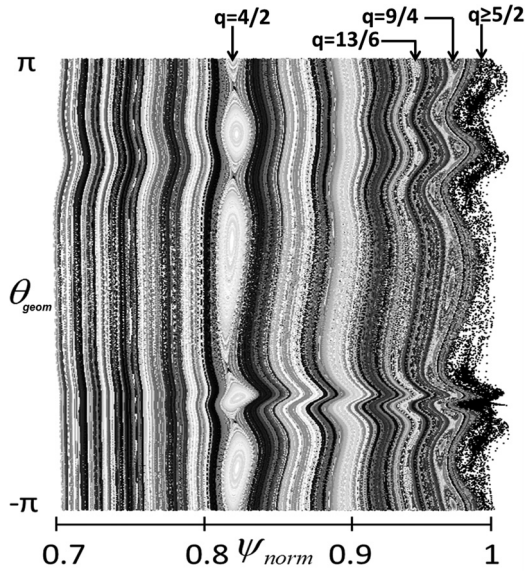

FIG. 13. Poincaré plot of the magnetic topology in (ψ_0, θ_{geom}) coordinates ($\eta_0 = 10^{-7}$, $\tau_{IC} = 10^{-3}$).

the modes generates secondary islands on the rational surface $q = 9/4$ and even tertiary islands on $q = 13/6$ (Ref. 27, Fig. 13). The observation of these secondary and tertiary islands can be explained by the flat q-profile in this area (Fig. 1), since the island size is inversely proportional to the magnetic shear $dq/d\psi$. The secondary islands are the result of the non-linear coupling between the $n = 2$ mode with itself whilst the tertiary islands correspond to the coupling between this resulting $n = 4$ component with $n = 2$. Even though the $n = 4$ and $n = 6$ modes are not explicitly included in these simulations, they appear nonetheless as a result of non-linear couplings.

From the resistivity scan and the progressive addition of the different flows, we find that the diamagnetic rotation and the resistivity are the two main parameters affecting the penetration of the RMPs, and three different regimes are identified depending on these two parameters (Fig. 16).

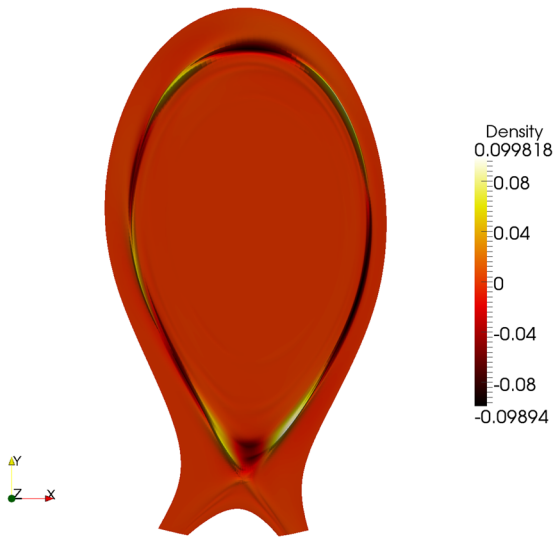

FIG. 14. $n = 2$ density perturbation with RMPs, mainly located on the resonant surface $q = 5/2$ ($\eta_0 = 10^{-7}$, $\tau_{IC} = 10^{-3}$).

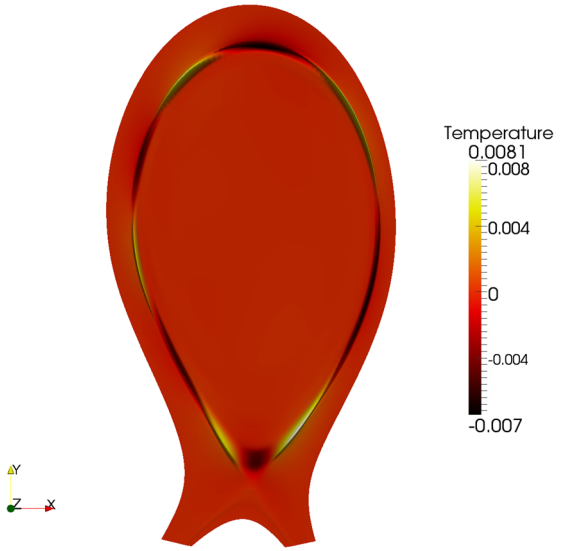

FIG. 15. $n = 2$ temperature perturbation with RMPs, mainly located on the resonant surface $q = 5/2$ ($\eta_0 = 10^{-7}$, $\tau_{IC} = 10^{-3}$).

At low diamagnetic rotation ($\tau_{IC} = 10^{-3}$, which is half the realistic value) and high resistivity ($\eta_0 = 10^{-7}$), the generated islands rotate in the ion diamagnetic direction at the ion poloidal rotation frequency $f^* \sim m\frac{V_\theta}{2\pi r_{res}}$, where m is the poloidal mode number corresponding to the resonant surface. The main poloidal mode generated being the mode $m = 5$ (Figs. 14 and 15), the oscillation of the magnetic energy of the mode $n = 2$ (Fig. 16) mainly corresponds to the rotation of the magnetic islands on the surface $q = 5/2$ at the frequency $f^* \sim 6$ kHz. The amplitude of these islands oscillates at the same frequency f^*: indeed, while they are rotating with the plasma, they successively face maxima and minima of external static magnetic perturbations, which explains the fluctuation of the island size at the frequency f^*. This mode is probably related to the Rutherford regime described in the Fitzpatrick theory[16] and such an oscillating regime is also found in simulations with toroidal rotation included.[28] Small fluctuations of the SOL density and temperature are observed

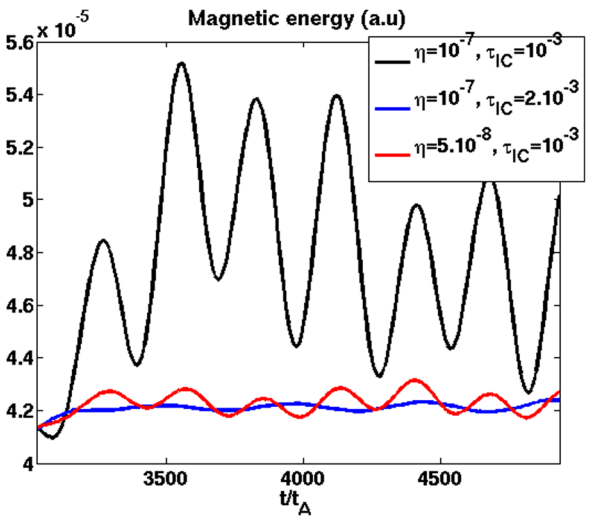

FIG. 16. Three different regimes of penetration of the RMPs: magnetic energy of the mode $n = 2$ depending on the diamagnetic parameter τ_{IC} and the plasma resistivity η_0.

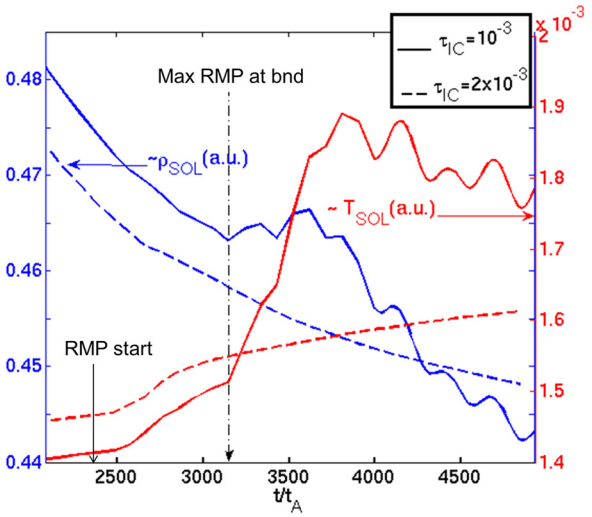

FIG. 17. Volume integrated electron density and temperature in the scrape-off layer at resistivity $\eta_0 = 10^{-7}$ for two different diamagnetic velocities ($\tau_{IC} = 10^{-3}$ and 2×10^{-3}).

in this regime to rotate at the same frequency as the magnetic flux fluctuations (Fig. 17, solid line). Note that the volume integrated density and temperature in the SOL increase when switching on the RMPs, suggesting an enhancement of the density and heat transport due to the formation of an ergodic region at the edge (Fig. 13). However, no significant changes in plasma density and temperature profiles were observed in modeling; the density pump-out has not been observed so far: less than 1% of the pedestal density is lost in the simulations, as compared to up to 20% in the experiments.[3,6] The regime of oscillating islands is possibly related to the ELM suppression regimes at high collisionality (characterized by a smaller pedestal, a smaller diamagnetic rotation and a high

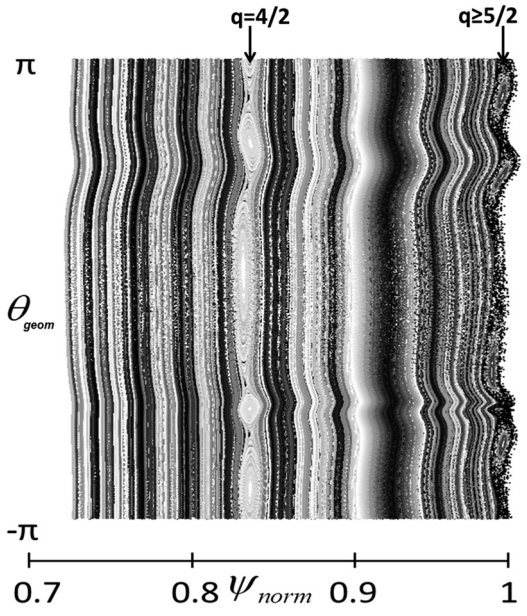

FIG. 18. Poincaré plot of the magnetic topology in (ψ_0, θ_{geom}) coordinates at larger diamagnetic rotation $\tau_{IC} = 2 \times 10^{-3}$ (resistivity is kept $\eta_0 = 10^{-7}$). Note that the islands generated by the RMPs are smaller compared to Fig. 13, which points out the larger screening induced by the large diamagnetic (poloidal) rotation.

resistivity[4,29]), but more modeling of realistic experimental cases is needed to confirm this statement.

At larger diamagnetic rotation ($\tau_{IC} = 2 \times 10^{-3}$, corresponding to the realistic value) and high resistivity ($\eta_0 = 10^{-7}$), the driven mode is on the contrary static and "locked" to the external RMPs. The Poincaré plot (Fig. 18) shows that the islands generated on the rational surface $q = 4/2$ are smaller at larger τ_{IC}, which means that the RMPs are more screened by the diamagnetic flow. As for the secondary and tertiary islands, they are totally invisible in this case. Consistently, the magnetic energy of the mode $n = 2$ is decreased as compared to the oscillating case (Fig. 16). Nonetheless, an ergodic layer is formed at the very edge (for $\psi \geq 0.98$), but its width is smaller and the deformation of the boundary is reduced. The heat transport, slightly enhanced by RMP application (as suggested by the increase in SOL temperature in Fig. 17, dash line), is weak compared to the previous case, due to the smaller ergodization of the edge.

An intermediate regime is also found at lower resistivity ($\eta_0 = 5 \times 10^{-8}$) with $\tau_{IC} = 10^{-3}$: the magnetic islands are quasi-static and slightly oscillate at the ion poloidal rotation frequency. The screening level is approximately the same as in the static case.

RMP screening is quantified in these three cases in Fig. 19, where the Fourier harmonics ($n = 2, m = 3 - 6$) of the magnetic flux perturbation are plotted. In the three cases, the central islands ($m = 3 - 4$) are screened on the corresponding resonant surfaces. Yet the Fourier harmonics $|\psi_{mn}|$ ($m = 3 - 4$) do not totally vanish on the resonant surfaces (which is consequent with the formation of small islands on $q = 4/2$), contrary to the previous modeling in cylindrical geometry[12] where the central harmonics were totally screened. The discrepancy between cylindrical and toroidal modeling is not really understood, but will be discussed in Sec. IV. Regarding the edge harmonics ($m = 5 - 6$), the amplitude of the Fourier harmonics $|\psi_{mn}|$ is 2–3 times lower in the cases at low resistivity or high diamagnetic rotation than

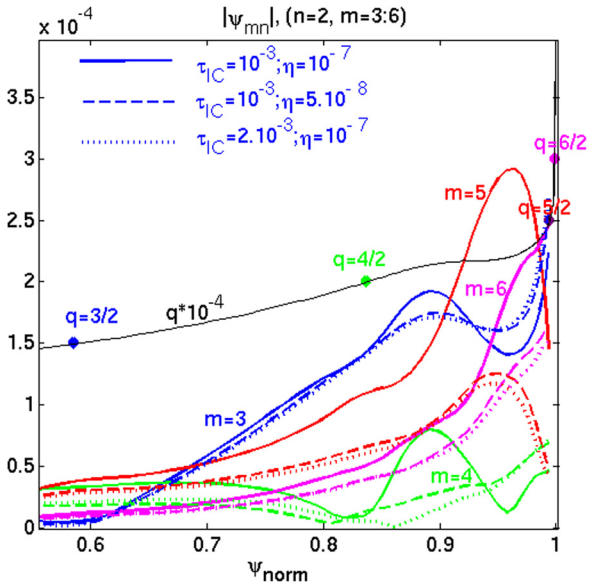

FIG. 19. Fourier harmonics of the magnetic flux ($n = 2, m = 3 - 6$) depending on the resistivity and the diamagnetic rotation for $t \sim 4950 t_A$.

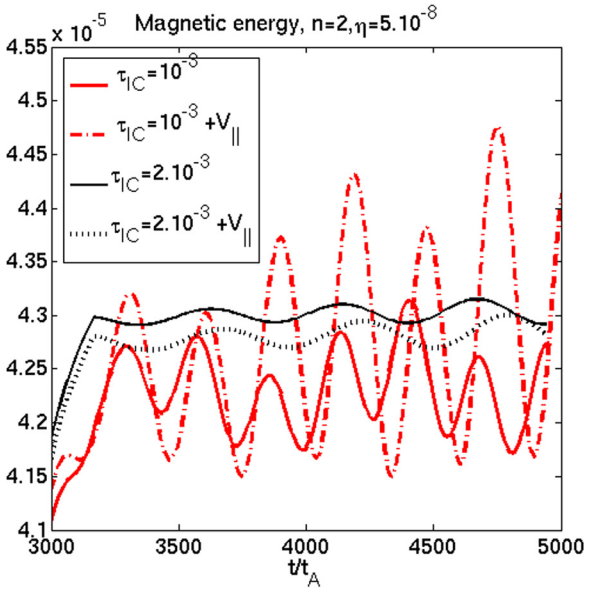

FIG. 20. Effect of the source of parallel rotation on the magnetic energy of the driven mode $n=2$ (resistivity $\eta_0 = 5 \times 10^{-8}$) at low ($\tau_{IC} = 10^{-3}$) and high ($2 \times 10^{-3}$) diamagnetic rotation.

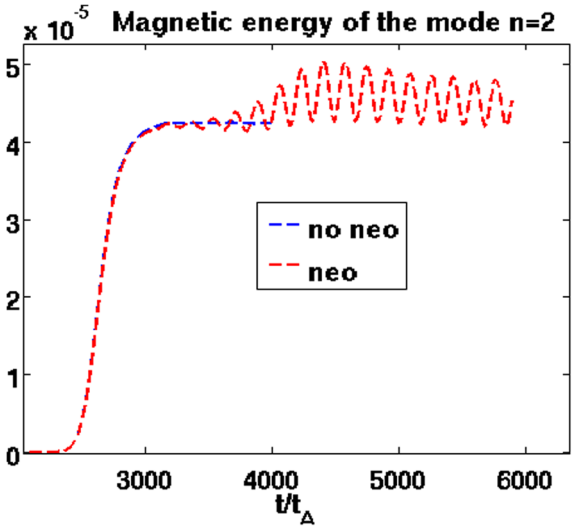

FIG. 21. Effect of the neoclassical friction on the magnetic energy of the driven mode $n=2$ (resistivity $\eta_0 = 10^{-7}$) at large diamagnetic rotation (2×10^{-3}). Without neoclassical effects in the model (in blue), the islands are static. With neoclassical friction included (in red), the generated islands are first static but finally rotate at the ion perpendicular rotation frequency.

it is in the oscillating case, which means that the corresponding island size, proportional to $|\psi_{mn}|^{1/2}$, is reduced.

From now, the source of parallel momentum is added in the model. If the screening effect provided by high diamagnetic rotation and/or low resistivity is clear in the JET case, the effect of the parallel rotation is more complex (Fig. 20). As the parallel rotation does not directly affect the screening of RMPs, an increased parallel rotation does not necessarily imply an increased screening of RMPs. Indeed, at low resistivity ($\eta_0 = 5 \times 10^{-8}$), in the slightly oscillating regime characterized by low diamagnetic rotation ($\tau_{IC} = 10^{-3}$), the parallel rotation increases both the average island size and the fluctuation of the island width: this can explain the larger fluctuation of the magnetic energy of the mode $n=2$ in Fig. 20. The oscillation frequency of the islands is also modified by the parallel rotation, probably because of the induced change in the radial electric field and the poloidal rotation. On the contrary, at higher diamagnetic rotation ($\tau_{IC} = 2 \times 10^{-3}$), the energy of the mode $n=2$ is lower when the parallel velocity source is added, showing a slightly stronger screening by parallel velocity.

Last, in our simulations with the realistic diamagnetic rotation ($\tau_{IC} = 2 \times 10^{-3}$) and the source of parallel rotation (at $\eta_0 = 10^{-7}$), the addition of the neoclassical effects in the model modifies the plasma response. For a same simulation without neoclassical friction, the magnetic islands generated on $q = 5/2$ are static; however, with neoclassical effects, the generated islands are first static and then progressively rotate in the ion flow direction, until they reach the ion perpendicular rotation frequency f^* (Fig. 21). The island width also oscillates at the frequency f^*. We are thus in the same regime of plasma response as for the case at low diamagnetic rotation. The change in the regime of plasma response is not due to a modified perpendicular rotation (in both cases without and with neoclassical effects, the perpendicular velocity is the same at the vicinity of the resonant surface $q = 5/2$). The reason why this regime is obtained at large diamagnetic rotation with neoclassical friction is not really understood, but it may be explained by a change in viscosity resulting from the balance between the neoclassical friction force and the viscous force in the momentum equation. More modeling would be necessary to give a global interpretation of the phenomena at stake. The Poincaré plot of the magnetic topology of this case is given in Fig. 22. Compared to Fig. 18 (case without source of parallel rotation or neoclassical friction), the

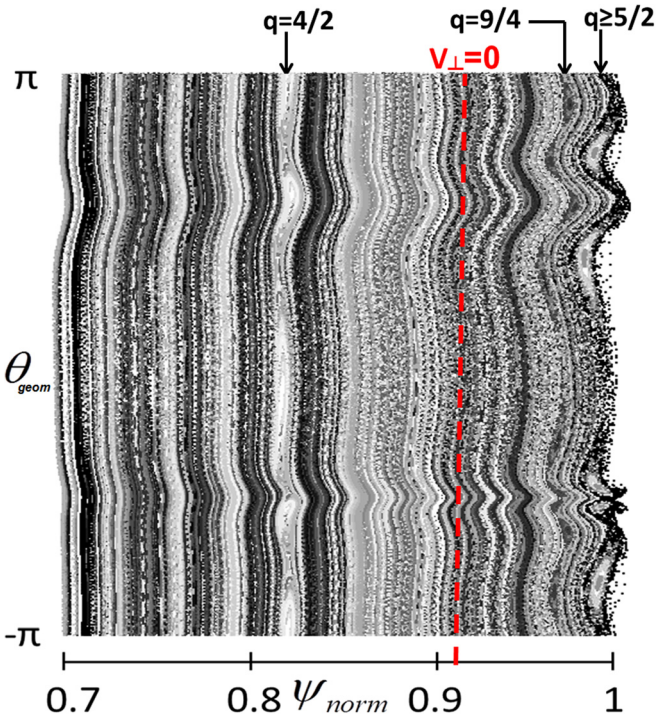

FIG. 22. Poincaré plot of the magnetic topology in (ψ_0, θ_{geom}) coordinates with diamagnetic rotation ($\tau_{IC} = 2 \times 10^{-3}$), parallel source of rotation and neoclassical friction (resistivity $\eta_0 = 10^{-7}$). The surface where the perpendicular velocity $V_\perp$ cancels (indicated by the red dashed line) does not match a resonant surface, which explains that the RMPs do not fully penetrate.

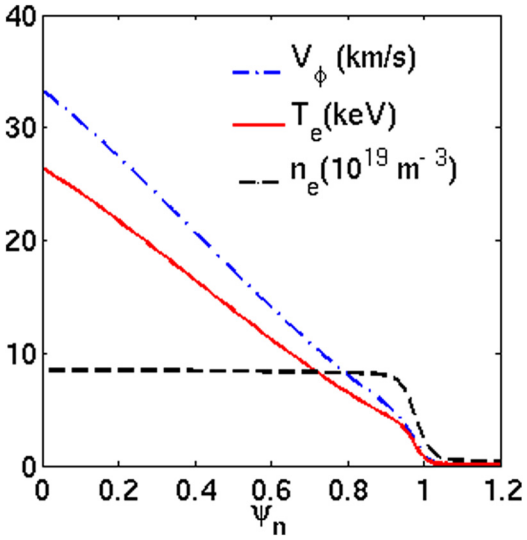

FIG. 23. ITER input density, temperature and toroidal rotation profiles.

island width and the size of the ergodic layer are similar. Actually, in all cases, the position where perpendicular velocity cancels (red dashed line in Fig. 22) is located between $q = 4/2$ and $q = 5/2$ and does not match a resonant surface. It explains why the perturbations significantly penetrate only at the very edge ($\psi \geq 0.97$) where resistivity is higher and where the perpendicular rotation is dominated by the diamagnetic effects.

IV. RMPs IN ITER

A. Input parameters and equilibrium plasma flows

In this section, the equilibrium and plasma parameters of the ITER standard H-mode scenario $15MA/5.3T$ are used. The machine dimensions are $R = 6.2\,\mathrm{m}$, $a = 2\,\mathrm{m}$ and the safety factor is $q_{95} = 3.5$. The density, temperature, and toroidal rotation profiles are given in Fig. 23. Central density is $n_{e,0} = 8 \times 10^{19}\mathrm{m}^{-3}$, central temperature is $T_0 = 27.8\,\mathrm{keV}$ and the initial toroidal rotation profile is similar to the temperature profile with a central arbitrary rotation frequency $\sim$0.9 kHz, which is in the range of the expected value in

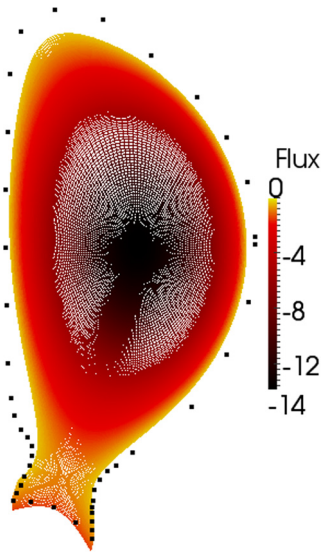

FIG. 24. ITER equilibrium flux-aligned mesh used in modeling.

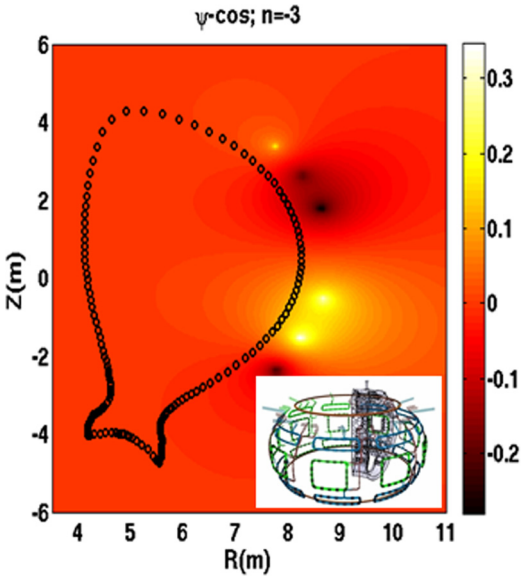

FIG. 25. Vacuum solution for the magnetic flux perturbation ($n = 3$, IVC at max $I_{coil} = 54kAt$) from the ERGOS code, JOREK boundary in black and sketch of the ITER RMP coils in the bottom right corner.

ITER. The flux-aligned mesh used for modeling is given in Fig. 24. The resonant magnetic flux perturbations generated by In-Vessel Coils, in the configuration $n = 3$ and a current $I_{coil} = 54kAt$ (Fig. 25, Ref. 9) are calculated from the vacuum code ERGOS[23] and are applied as boundary conditions in $10^3 t_A$ in the same way as in Sec. III.

Equilibrium plasma flows are computed for a central resistivity $\eta_0 = 10^{-8}$, which is, for numerical reasons, 100 times higher than the normalized Spitzer value calculated for ITER ($\eta_0 = 10^{-10}$). As the diamagnetic parameter is inversely proportional to $F_0 = R_0 B_{\varphi 0}$, the value for ITER $\tau_{IC} = 5 \times 10^{-4}$ is 4 times smaller than in the JET simulation. Neoclassical coefficients are taken constant in this part for simplicity: $\mu_{neo} = 10^{-5}$ and $k_i = -1$.[12] The profiles of the parallel, poloidal, and neoclassical velocities along the midplane are given in Fig. 26. The equilibrium radial electric

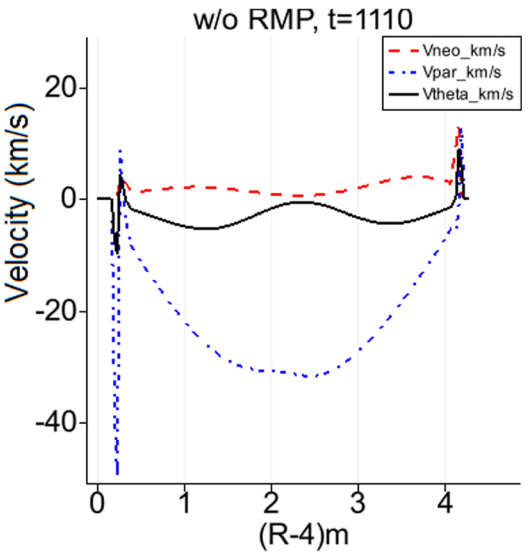

FIG. 26. Profiles of the parallel, poloidal, and neoclassical velocities along the midplane in ITER simulations.

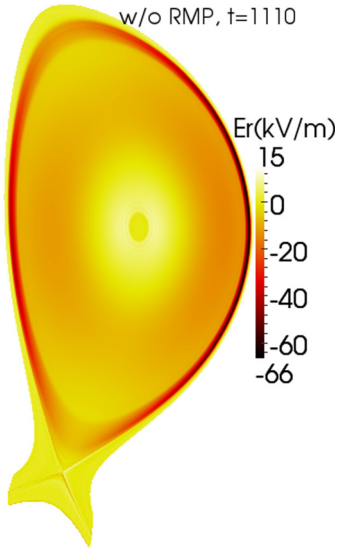

FIG. 27. 2D-profile of the radial equilibrium electric field in ITER (without RMPs).

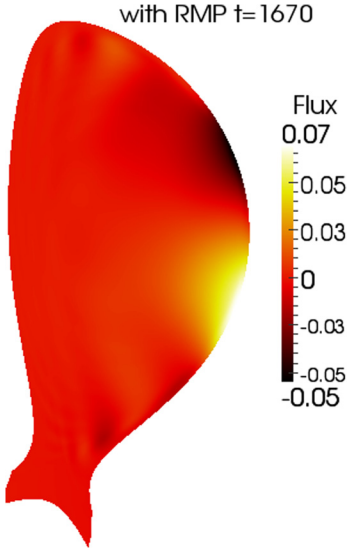

FIG. 29. Static $n=3$ magnetic flux perturbation due to RMPs in ITER.

field $E_r = -\nabla_\perp u \cdot \nabla\psi/|\nabla\psi|$, with the characteristic well in the pedestal, is plotted in Fig. 27.

B. RMP screening in ITER

When the RMPs are not activated, the mode $n=3$ remains stable: as shown in Fig. 28, the magnetic energy of the mode $n=3$ is negligible. When RMPs are switched on (Fig. 25) at the boundary of the computational domain, the energy of the $n=3$ toroidal harmonic grows until it saturates, corresponding to the saturation of the size of the magnetic islands generated by the RMPs on the resonant surfaces $q = m/3, m \geq 4$. These magnetic islands are static: they are "locked" to the external RMPs and their size is constant. The magnetic flux perturbation $n=3$ is given in Fig. 29. The plasma response is manifested by a perturbation of the parallel current induced on the resonant surfaces (Fig. 30). The perturbation of density (Fig. 31) and temperature (Fig. 32) mainly develops at the very edge ($q = m/3, m \geq 10$) where the resistivity is higher; on the more internal resonant surfaces ($q = 4/3 \rightarrow 9/3$), the perturbation vanishes, which means that the central harmonics are screened. The temperature and density perturbations and the stochastization of the edge (for $\psi \geq 0.96$, as shown in the Poincaré plot, Fig. 36) slightly increase the edge heat and particle transport, resulting in a small degradation of the pedestal (Fig. 33).

The profiles of the Fourier coefficients of the magnetic perturbation $\psi_{m,n}$ calculated with JOREK in presence of the plasma response are compared to the coefficients calculated in the vacuum with the code ERGOS. Compared to the vacuum case,[12] the central harmonics $m = 4-9$ (Figs. 34 and 35) are screened by the rotating plasma on the corresponding resonant surfaces $q = m/n$. Yet it is important to note that the screening of the resonant part of the magnetic

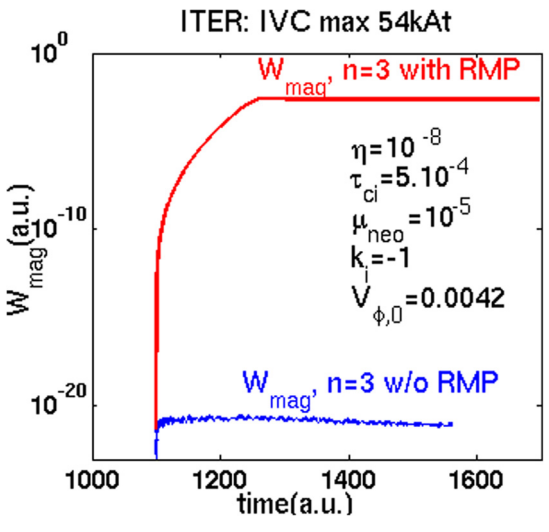

FIG. 28. Magnetic energy of the $n=3$ mode without/with RMPs.

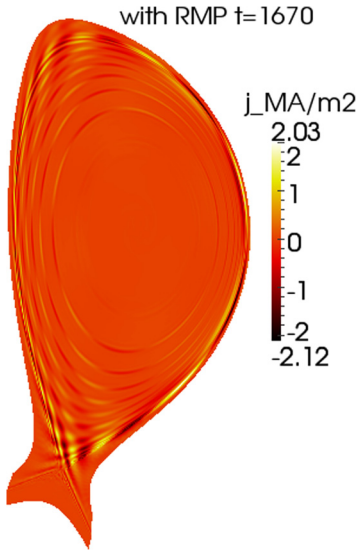

FIG. 30. $n=3$ toroidal current perturbation appearing in response to RMPs in ITER.

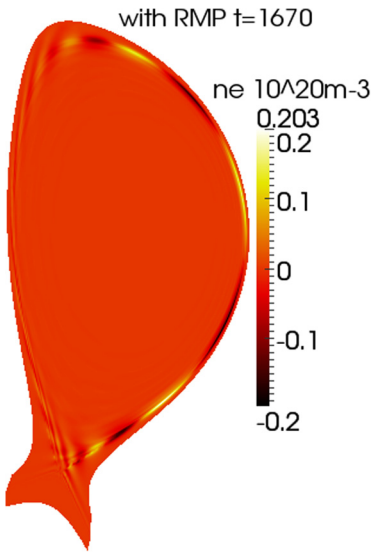

FIG. 31. $n = 3$ density perturbation due to RMPs in ITER.

perturbations is only partial and that the screening factor $|\psi_{m,n}|/|\psi_{m,nvacuum}|$ on the resonance reaches $\sim 10\%$ for $m = 4 - 9$. This partial penetration is consistent with the fact that small magnetic islands are formed on the resonant surfaces (Fig. 36). The screening factor is much larger here than in the cylindrical modeling where the resonant component was reduced under 1%.[12] Comparatively, other simulations made with toroidal codes[13,14] also found a similar screening factor ($\sim 10\% - 20\%$), which is $1 - 2$ orders of magnitude larger than the results in cylindrical approximation[11,12,30] and in the analytical calculations from layer theory.[31] The discrepancy between modeling in realistic geometry and simpler models is not yet understood. Several parameters, such as toroidal effects, compressibility or differences in resistivity, and viscosity, might explain this discrepancy. Another phenomenon pointed out in toroidal simulations (Figs. 34 and 35 and Ref. 14) is the amplification of the non-resonant harmonics due to the so-called resonant

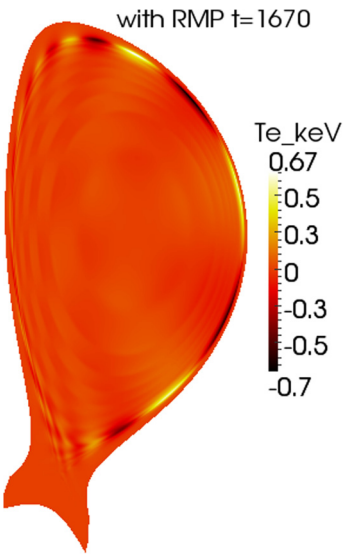

FIG. 32. $n = 3$ temperature perturbation due to RMPs in ITER.

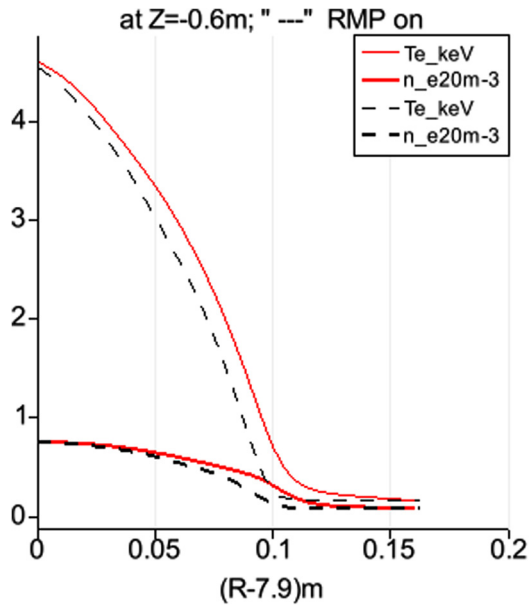

FIG. 33. Density and temperature profiles at the edge for $Z = -0.6$m without (full line) and with RMPs (dash).

field amplification (RFA). Indeed, the amplitude of the magnetic perturbations in the core is larger with plasma response than in the vacuum modeling, due to the resonant response of a marginally stable kink mode.[32] At the edge, the amplitude of the resonant harmonics $m = 10 - 11$ (Fig. 35) has the same order of magnitude in both vacuum and plasma cases. The magnetic perturbation thus significantly penetrates only at the very edge where the resistivity is the highest, which is similar to the cylindrical non-linear MHD modeling results.[12]

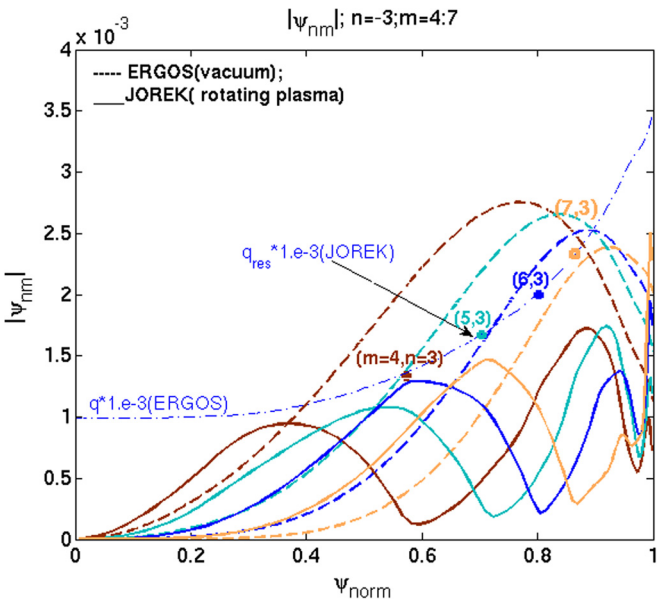

FIG. 34. Fourier harmonics of the magnetic flux perturbation $|\psi_{m,n}|$, $n = 3$, $m = 4 - 7$ in the vacuum case (ERGOS code, dash) and taking into account the plasma response (JOREK, full line). The q-profile is given and the positions of the resonant surfaces are indicated by the dots. Note that compared to the vacuum case, all these harmonics $m = 4 - 7$ are screened on the corresponding resonant surfaces $q = m/n$ in the presence of the rotating plasma.

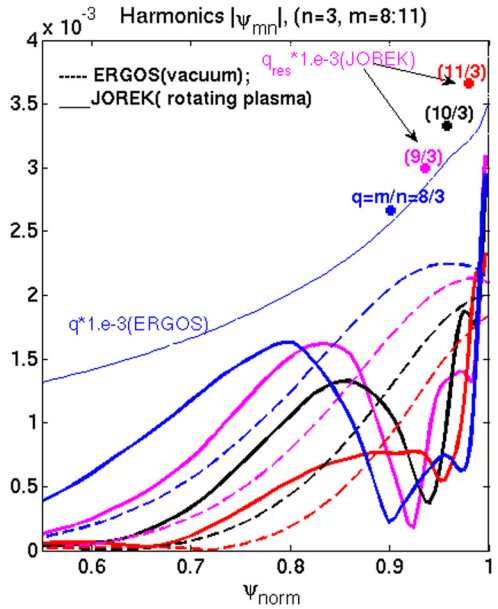

FIG. 35. Fourier harmonics of the magnetic flux perturbation $|\psi_{m,n}|$, $n = 3$, $m = 8 - 11$ in the vacuum case (ERGOS code, dash) and taking into account the plasma response (JOREK, full line). The q-profile is given and the positions of the resonant surfaces are indicated by the dots. The edge harmonics $m = 10 - 11$ have a comparable amplitude on the resonant surfaces $q = 10 - 11/3$ in the ERGOS and JOREK cases, showing the penetration of these harmonics in the plasma.

C. Stochasticity at the edge

The RMP penetration at the edge generates the formation of islands on the resonant surfaces $q = m/3, m \geq 10$. As the edge resonant surfaces are close to each other due to strong magnetic shear, the islands overlap and therefore form an ergodic layer at the edge for $\psi \geq 0.96$, as suggests the Poincaré plot of the magnetic topology in (ψ, θ) coordinates Fig. 36.

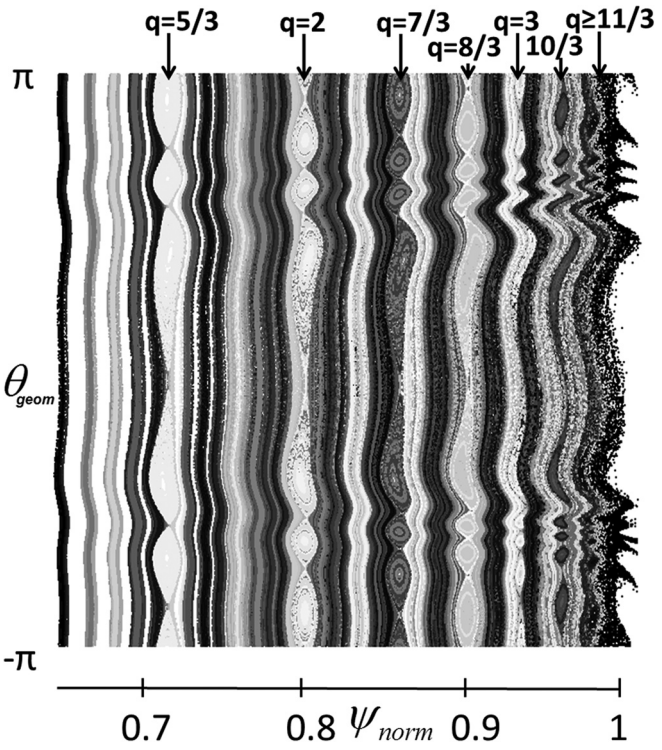

FIG. 36. Poincare plot of the magnetic topology with RMPs in (ψ_0, θ_{geom}) coordinates: magnetic field lines (starting at the edge inside the separatrix) integration after 200 toroidal turns at $\varphi = 0$. Resonant surfaces $q = m/3, m \geq 5$ are indicated. A stochastic layer is formed for $\psi \geq 0.96$.

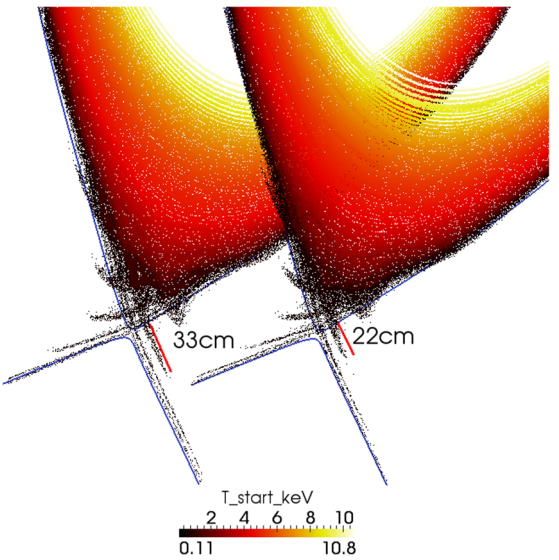

FIG. 37. Magnetic topology near the X-point in (R, Z) coordinates. A lobe structure characteristic of the ergodicity in X-point geometry is observed. On the left, a RMP simulation without neoclassical, diamagnetic flows or toroidal rotation is run for a central resistivity $\eta_0 = 10^{-7}$. On the right, the same RMP simulation is run with all flows included for a central resistivity $\eta_0 = 10^{-8}$: the resulting lobe size is smaller by 1/3 compared to the case without flows.

The formation of the ergodic layer is correlated with a splitting of the separatrix.[33] The separatrix under the RMP transforms into a homoclinic tangle defining the plasma edge,[34] manifesting itself as lobe structures (~20 cm) near the X-point (Fig. 37) and by smaller finger-like structures (~6 cm) at the top of the plasma (Fig. 38). The superposition of the magnetic topology with the plot of the homoclinic tangles (stable and unstable) defining the deformation of the separatrix is given in Fig. 39. These lobes near the X-point are observed in the experiments, either directly[35,36] or as the footprints of high heat and/or particle fluxes where the lobes

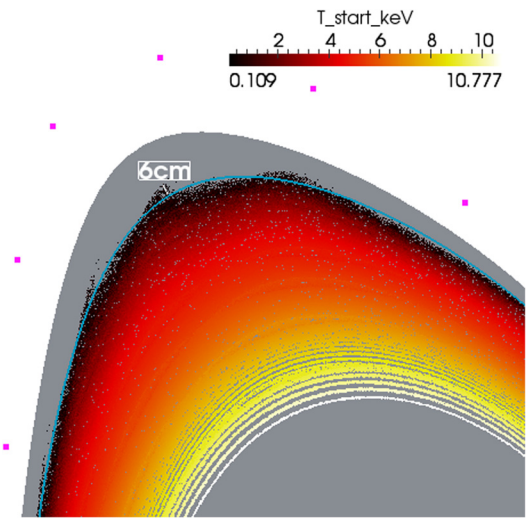

FIG. 38. Magnetic topology at the top of the machine. Small deformations of the separatrix (~6 cm) are observed.

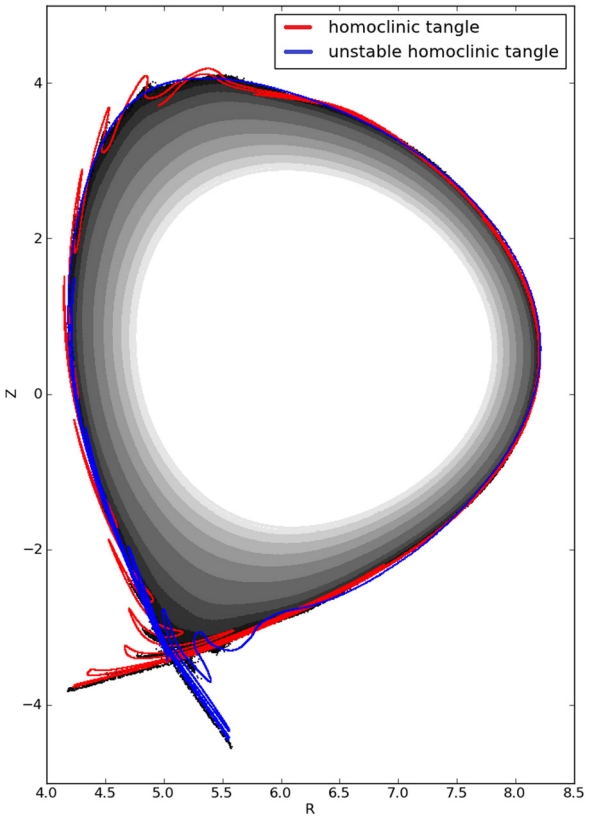

FIG. 39. Superposition of the Poincaré plot of the magnetic topology in (R,Z) coordinates with the stable (red) and unstable (blue) homoclinic tangles defining the deformation of the separatrix.

intersect the divertor.[37–40] Models of plasma response based on a simplified assumption of screening currents on resonant surfaces[41] or on a linear MHD model[42] predict significant shortening of the lobes when the RMP is screened by the plasma response. Shortening is observed in the magnetic field topology[40–42] and through the reduction of fluxes[43,44] and generally increases with the increase of the width of the plasma region where the RMP is screened.[41] The shortening of lobes currently represents the most convenient way to quantify experimentally the screening of RMPs. In the same way, in our simulations, the size of the lobes qualifies the screening of the RMPs by plasma flows. In Fig. 37, a simulation with the

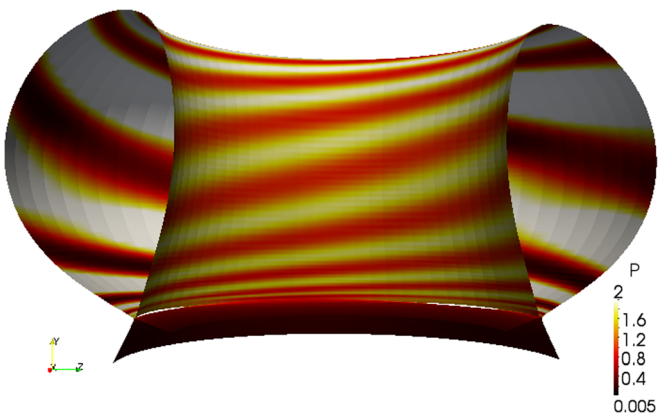

FIG. 40. 3D-plot of the pressure on an initial equilibrium flux surface without RMP near the separatrix. The 3D-deformation corresponds to a mode $(n = 3, m \sim 12)$.

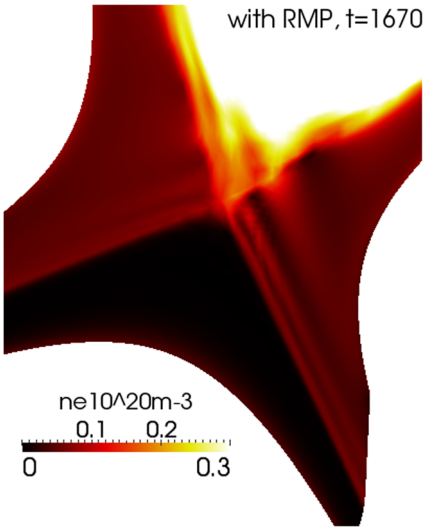

FIG. 41. Degradation of the density profile near the X-point due to RMPs.

same input RMP amplitude is run in two cases: with SOL flows only (induced by sheath conditions) and with all flows included (neoclassical and diamagnetic flows, source of toroidal rotation). The addition of the flows in the simulation shortens the length of the lobe structures near the X-point by $\sim 1/3$, which corroborates the hypothesis (so far deduced from simpler models) that the RMP screening by plasma flows is correlated to lobe/footprint shortening.

A 3D-deformation of the density, temperature and pressure profiles is observed. The deformation of the pressure profile close to the separatrix is found to be due to the mode $(n = 3, m \sim 12)$, Fig. 40. A small degradation of the density and temperature profiles is also observed near the X-point when RMPs are applied. The comparison of the density profile with (Fig. 41) and without RMPs (Fig. 42) shows the enhancement of the particle transport towards the divertor targets by the RMPs. A similar enhancement of the heat transport is observed. This increase in heat and particle fluxes subsequently generates a small splitting of the strike points on the divertor targets, mostly on the outer target (Fig. 43).

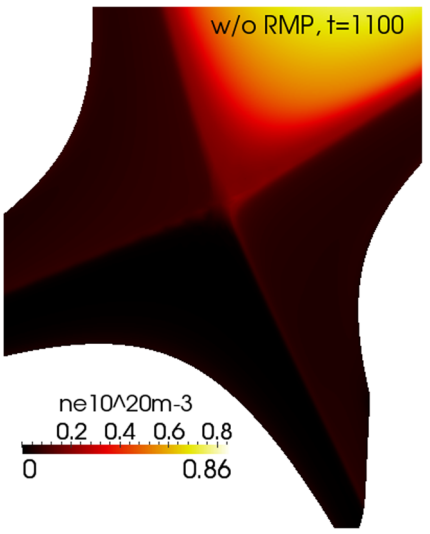

FIG. 42. Density near the X-point without RMPs.

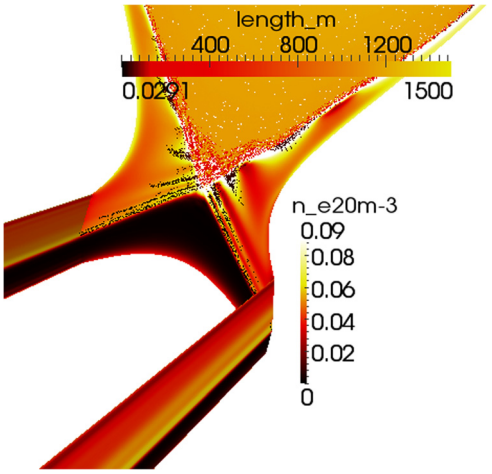

FIG. 43. 2D-Poincaré plot (in the poloidal plane) of the magnetic topology (connection length) near the X-point, plotted together with the electron density on the divertor targets (toroidal section). Note the induced splitting of the strike points on the outer divertor target.

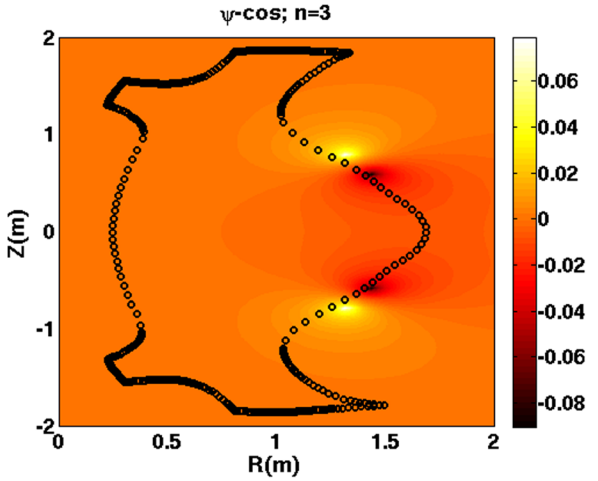

FIG. 45. Input resonant magnetic perturbation generated by the RMP coils calculated in the vacuum with the ERGOS code and applied as boundary conditions of the computational domain (in black).

V. FIRST SIMULATIONS IN MAST DOUBLE NULL DIVERTOR (DND) CONFIGURATION

A. Input parameters

RMP penetration in MAST is studied in Double Null Divertor configuration with plasma parameters corresponding to the shot #24763 (previously considered in Ref. 45). The central density is $n_{e,0} = 4.25 \times 10^{19}\mathrm{m}^{-3}$, the central electron temperature is $T_{e,0} = 1.04\,\mathrm{keV}$ and the central resistivity is taken $\eta_0 = 10^{-7}$ (this is two orders of magnitude larger than the normalized Spitzer value). The disposition of the RMP coils chosen is the "90L" configuration, since it corresponds to a maximal amplitude of the radial magnetic field (generated by the RMPs) located on the resonant surfaces, as shown in Fig. 44. The $n = 3$ Fourier component of the vacuum RMP field imposed at the boundary of the computational domain is given in Fig. 45. For numerical reasons, in the simulation the current circulating in the RMP coils is taken to be $1/10$ of the experimental value. The reason is that during the transitory phase when RMPs are switched on progressively at the boundary, toroidal currents $J = \Delta\psi$ appear close to the boundary and dissipate when the stationary solution is reached. If the RMP amplitude is too large, these toroidal currents evolve on a very fast time scale, setting a stringent constraint on the allowed time step. For the moment, we did not succeed in optimizing the numerical scheme for the realistic MAST parameters.

Two different cases are studied and compared: first, the simulation is run with only the SOL flows generated by sheath conditions. Second, the diamagnetic effects are added, with a diamagnetic parameter $\tau_{IC} = 10^{-2}$ (note that the large rotation in MAST implies a realistic diamagnetic parameter $\tau_{IC} = 5 \times 10^{-2}$, i.e., 100 times the one of the ITER case, but a lower value is taken here for numerical reasons: as the very large value of τ_{IC} again imposes a severe constraint on the time step, we opted here for intermediate well resolved values; realistic values are left for future work). In this section, neither the source of parallel rotation nor the neoclassical

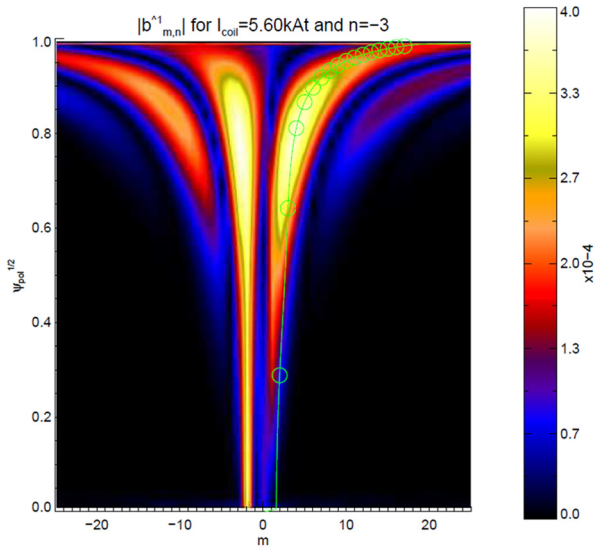

FIG. 44. Fourier harmonics of the radial magnetic field generated by the RMP coils in disposition 90L: in this configuration, the magnetic perturbation is maximal on the resonances $(m, n = 3)$.

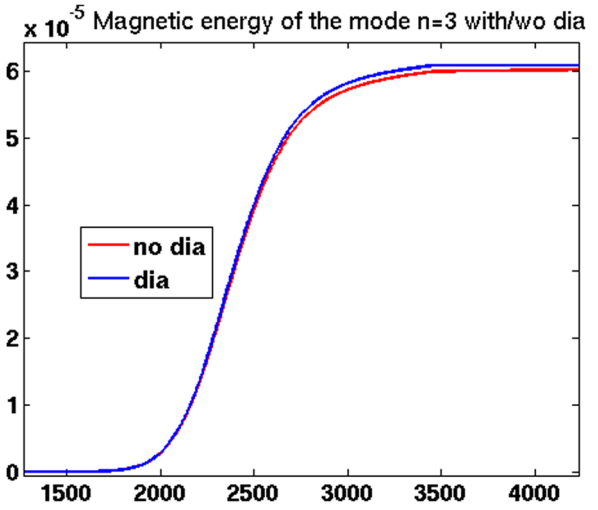

FIG. 46. Magnetic energy of the mode $n = 3$ driven by RMPs in the 2 cases: without and with diamagnetic effects.

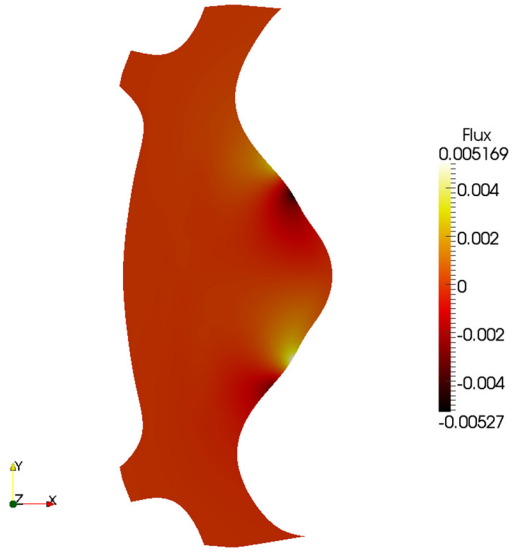

FIG. 47. Magnetic flux perturbation penetrating in the plasma (without diamagnetic effects).

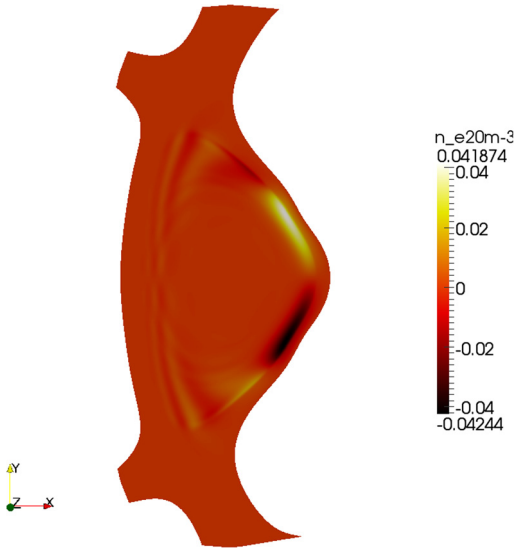

FIG. 49. Density perturbation with $n = 3$ RMPs in MAST (without diamagnetic effects).

poloidal friction is included in the model so as to focus on the effects of the diamagnetic rotation on RMP penetration.

B. RMP penetration

In both cases (with or without diamagnetism), a static $n = 3$ mode grows due to the RMPs (Fig. 46). The magnetic energy of the mode is a few percent higher in the case including the diamagnetic flow, which means that the diamagnetic effects slightly amplify the magnetic perturbations in this MAST configuration.

The penetration of the magnetic flux perturbation is given in Fig. 47 and the induced current perturbations on the resonant surfaces are shown in Fig. 48 (case without diamagnetic flow). The electron density (Fig. 49) and temperature perturbations (Fig. 50, $n = 3$) represent up to 10% of the central average value and are mainly located at the edge on the LFS, at the proximity of the RMP coils.

The radial profiles of the Fourier harmonics of the magnetic flux perturbation $|\psi_{m,n}|$ ($n = 3$, $m = 4 - 12$), are presented in Figs. 51 and 52 for both cases with and without diamagnetic flow. In both cases, the central resonant harmonics $m = 4 - 9$ are screened near the corresponding surfaces $q = m/n$. The screening of the resonant harmonics is only partial (reduced to ~10% of the vacuum perturbation) and magnetic islands are thus generated on the resonant surfaces in both cases (without Fig. 53 and with diamagnetic effects Fig. 54). These islands are larger in the core plasma in the simulation without diamagnetic rotation: the amplitude of the low poloidal numbers is reduced by the rotation. Also the amplification of the non-resonant magnetic perturbation due to RFA is observed in the core. At the edge, the harmonics $m = 10 - 12$ penetrate in both cases, but the amplitude is larger in the diamagnetic case (Fig. 52): the diamagnetic flow seems to amplify the perturbation at the edge. Indeed

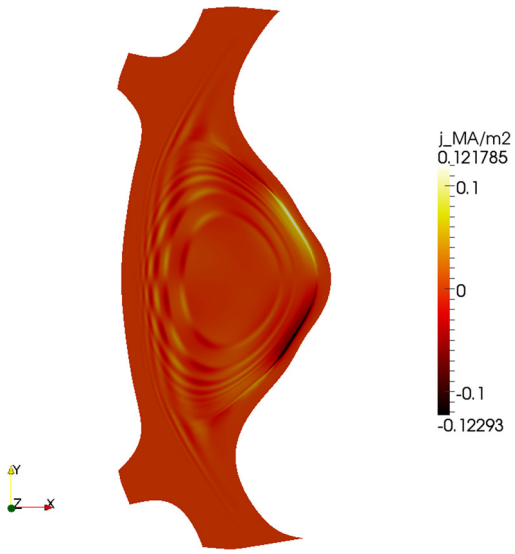

FIG. 48. Current perturbation generated on the resonant surfaces $q = m/n$, $n = 3$ (without diamagnetic effects).

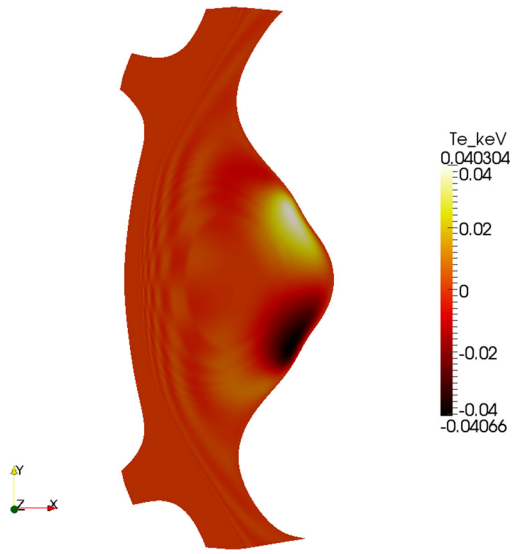

FIG. 50. Electron temperature perturbation with $n = 3$ RMPs in MAST (without diamagnetic effects).

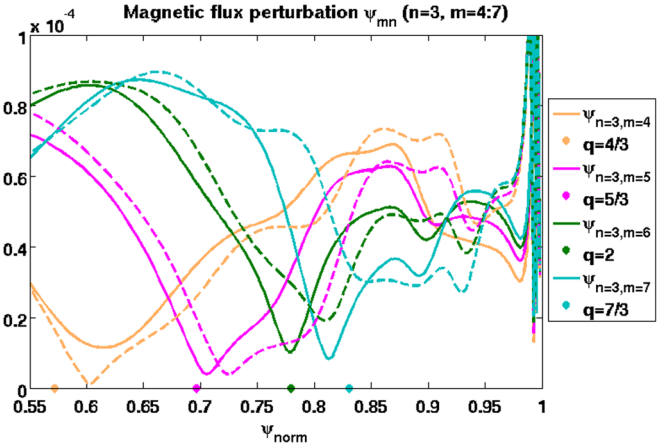

FIG. 51. Radial profile of the Fourier harmonics of the magnetic perturbation $|\psi_{m,n}|$, $m = 4-7$ in both cases: without diamagnetic effects (dash) and with diamagnetic effects included (full line). The approximate position of the resonant surfaces $q = m/n$ is represented by the dots. All the central harmonics $m = 4-7$ are screened near their corresponding resonant surfaces in both cases.

the resonant components of the Fourier harmonics $m = 9-12$ are slightly larger with diamagnetic effects on the corresponding resonant surfaces $q = m/n$ (Figs. 53 and 54).

C. Ergodization and 3D-effects

The penetration of the external RMP harmonics creates an ergodic layer at the edge for $\psi \geq 0.96$ (Figs. 53 and 54). Related to the ergodization are lobe structures formed near the X-point, as shown in Fig. 55 (case with diamagnetic flows included). It is interesting to notice that the presence of the two separatrices in DND configuration constrains the trajectories of the magnetic field lines so the lobes are only formed in the LFS. This phenomenon is also observed in MAST DND experiments with the fast camera. The size of the lobes in the LFS is comparable in both studied cases (with and without diamagnetic effects).

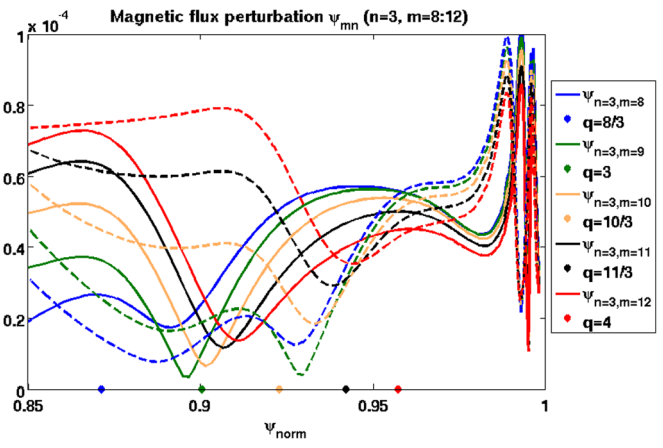

FIG. 52. Radial profile of the Fourier harmonics of the magnetic perturbation $|\psi_{m,n}|$, $m = 8-12$ in both cases: without diamagnetic effects (dash) and with diamagnetic effects included (full line). The approximate position of the resonant surfaces $q = m/n$ is represented by the dots. The more central harmonics $m = 8-9$ are screened near their corresponding resonant surfaces in both cases, whereas the external ones ($m = 10-12$) penetrate close to the surface $q = m/n$ in both cases but are slightly more amplified in the case including the diamagnetic effects.

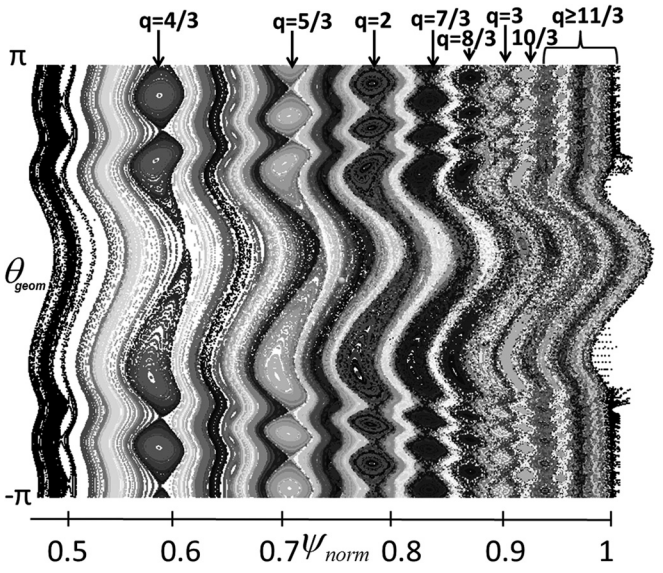

FIG. 53. Poincare plot of the magnetic topology in MAST without diamagnetic rotation, in (ψ_0, θ_{geom}) coordinates: magnetic field lines integration after 200 toroidal turns. The resonant surfaces $q = m/3, m \geq 4$ are indicated. A stochastic layer is formed for $\psi \geq 0.96$.

The 3D-deformation following a $n = 3$ toroidal mode number is observed in both simulations in the LFS. The separatrix is displaced towards the interior by a few centimeters at the midplane: $\sim 2-3$ cm without diamagnetism and ~ 1.5 cm in the diamagnetic case (Fig. 56) for a toroidal angle $\varphi = 0°$. The inward displacement of the electron density and temperature profiles at the midplane in the LFS (Fig. 57) is maximal for a toroidal angle $\varphi = 0°$ (position where the RMP coils deliver the largest negative flux perturbation) and minimal for $\varphi = 180°$ (angle where the maximal positive flux perturbation is applied). Compared to the density and temperature profiles without RMPs, the gradients are lower in the pedestal when the RMPs are applied, showing a

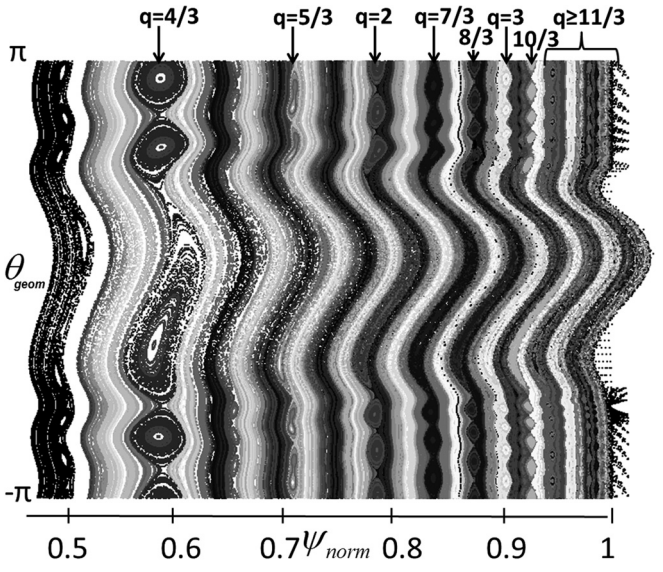

FIG. 54. Poincare plot of the magnetic topology in MAST with diamagnetic rotation included, in (ψ_0, θ_{geom}) coordinates: magnetic field lines integration after 200 toroidal turns. The resonant surfaces $q = m/3, m \geq 4$ are indicated. A stochastic layer is formed for $\psi \geq 0.96$.

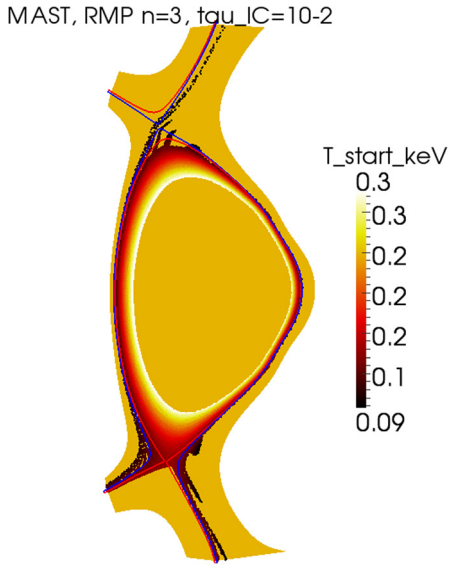

FIG. 55. Poincare plot of the magnetic topology with diamagnetic flow. The color represents the temperature of the starting point of the field line inside the separatrices. The length of the lobes near the X-points is sensibly the same in the case without diamagnetic flow.

small degradation of the confinement by the RMPs: this can be explained by the enhancement of the heat and particle transport due to the ergodicity at the edge. The 3D-corrugation of the electron density and temperature profiles are observed: the deformation of the temperature near the separatrix is given in Fig. 58.

Last, it is observed in the experiments that the radial electric field is made more positive by RMP application (Ref. 46). This phenomenon was found in simulations in the cylindrical case[12] and is also found in our toroidal simulations with JOREK, as plotted in Fig. 59 in the LFS (diamagnetic effects are included). The braking of the perpendicular electron velocity $V_{\perp,e}$ induced by RMPs is also evidenced in JOREK simulations (Fig. 60), following the same trend as in the experiments.[36,47] If the plasma brakes until $V_{\perp,e}$ becomes zero on the resonant surfaces, the magnetic perturbations are

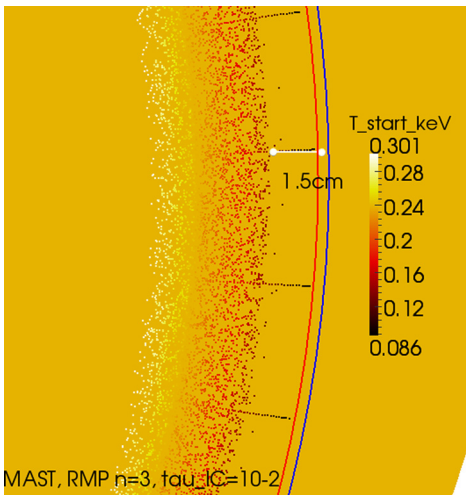

FIG. 56. Zoom in Poincare plot [Fig. 55] around the midplane (case with diamagnetic flow): the inward displacement of the last closed flux surface due to RMPs at the toroidal angle $\varphi = 0°$ is approximately 1.5 cm.

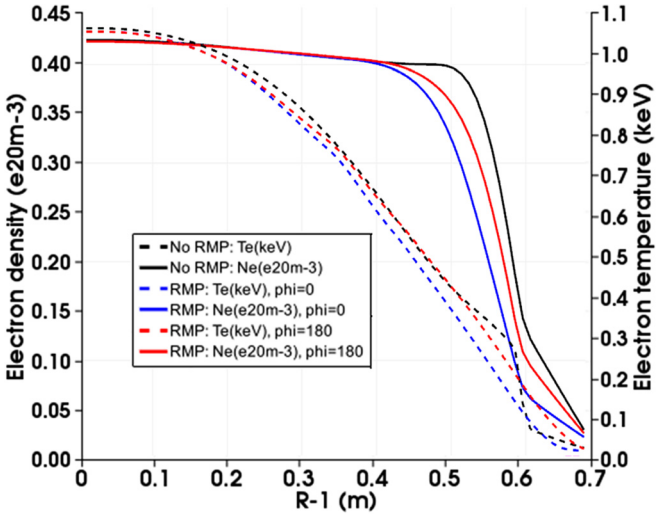

FIG. 57. Radial profiles of the electron temperature (dash) and the density (full line) at the midplane without RMPs (black), with RMPs at the toroidal angles $\varphi = 0°$ (blue) and 180° (red): note the small degradation of the pedestal and the 3D-deformation of density and temperature due to RMPs.

not screened on the resonant surfaces, as it was found in Refs. 11, 12, and 26 in cylindrical geometry and here demonstrated in Appendix for toroidal geometry. Fig. 60 shows that the damping of the perpendicular electron rotation occurs close to the resonant surface $q = 4/3$ ($\psi \sim 0.58$), which enables the growth of the $4/3$ magnetic islands (Fig. 54).

It is important to note that this study for the MAST case is a preliminary study and can only give trends of the effect of RMPs on the plasma in this particular case of a spherical tokamak in DND configuration. Clearly, the size of the displacements calculated here cannot be quantitatively compared to the experiments, since numerical limits imposed us to "minimize" two antagonist effects: on the one hand, the realistic RMP amplitude (10 times the one used in our simulations) should generate much larger penetration, on the other hand the realistic diamagnetic rotation (5 times the one used here) is likely to have much larger screening effects on the

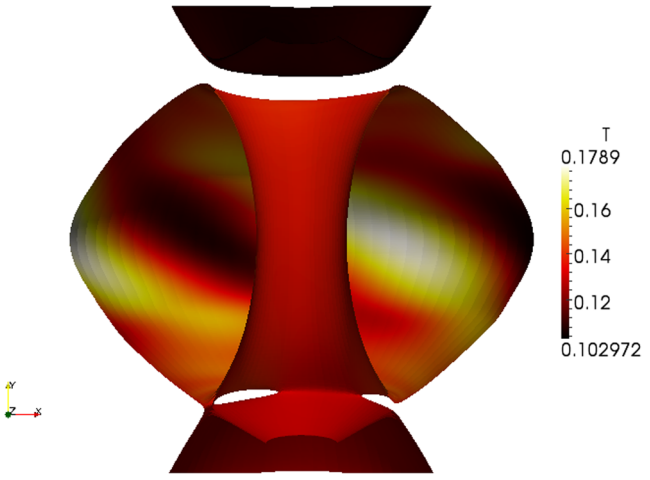

FIG. 58. 3D-deformation of the electron temperature near the separatrix due to RMPs.

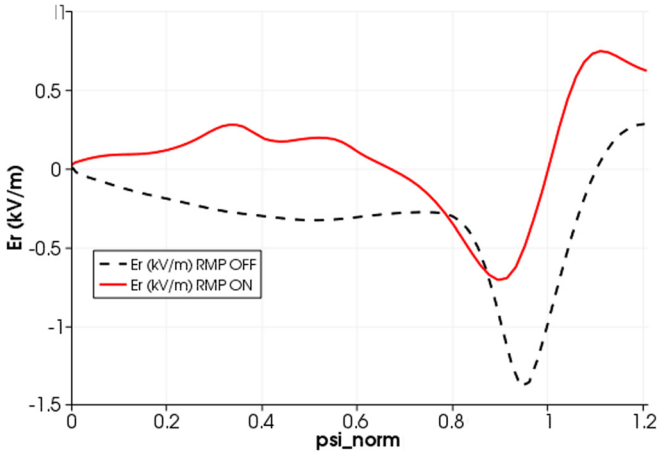

FIG. 59. Radial profile of the radial electric field at the midplane in the LFS without RMPs (dash black) and with RMPs (red).

RMPs. Anyway these results can be compared qualitatively to the experimental trends.

VI. CONCLUSION AND DISCUSSION

The penetration of the RMPs in the plasma was studied with the reduced MHD code JOREK, taking into account the plasma flows generated by the diamagnetic and neoclassical effects and a source of toroidal rotation. The screening of the RMPs on the resonant surfaces is observed in the center of the plasma in all the studied cases (JET, ITER, MAST) but the screening is only partial. The factor $|\psi_{m,n}|/|\psi_{m,n,vacuum}|$ on the resonances is 1–2 orders of magnitude larger than in the previous cylindrical modeling. The perturbation however significantly penetrates at the edge: magnetic islands grow on the resonant surfaces and eventually form an ergodic layer at the edge (for $\psi \geq 0.95$ in the three studied cases).

In JET geometry, a low plasma resistivity and a large diamagnetic rotation are found to increase the screening of the RMPs. Three regimes of RMP penetration are found depending on these two parameters: at low diamagnetic rotation and high resistivity, the generated islands co-rotate with the plasma ion flow and their size fluctuates at the same frequency. At larger diamagnetic rotation, the islands are static and "locked" to the external static RMPs; a stronger screening of the perturbations is observed. An intermediate regime is observed at lower resistivity, in which the generated island is quasi-static and slightly oscillate. The possible link between these regimes and the difference in ELM mitigation at high and low collisionality[3,29] is under investigation. As for the toroidal rotation, depending on the plasma parameters (in particular, on the resistivity), it can either increase or amplify the screening of the RMPs. Also, contrary to the JET case, the magnetic perturbation seems to be slightly amplified by the diamagnetic rotation at the edge in MAST simulations.

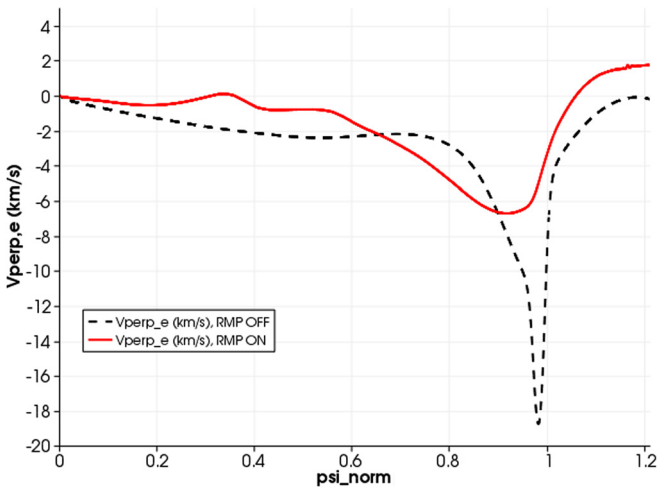

FIG. 60. Radial profile of the electron perpendicular velocity at the midplane in the LFS without RMPs (dash black) and with RMPs (red).

In MAST and ITER cases, static magnetic islands are formed on the resonant surfaces due to $n = 3$ magnetic perturbations. The presence of lobe structures related to the ergodization at the edge is evidenced in both cases ($\sim$20 cm in ITER, $\sim$7 cm in MAST). In ITER, the comparison of simulations run with and without flows demonstrates that the plasma rotation reduces the length of the lobes by $1/3$. The heat and particle transport is enhanced by the ergodicity near the X-point, resulting in the local degradation of the electron density and temperature profiles and the splitting of the strike points on the divertor targets, mostly in the LFS. In MAST, the separatrix follows a $(n = 3, m \sim 11)$ 3D-corrugation (the last close flux surface is moved inward by $\sim$1.5 cm at the midplane for a zero poloidal angle). The pedestal position follows the same inward movement, accompanied by a small degradation of the pedestal (relaxation of the density and temperature gradients). Last, the radial electric field evolution and the braking of the electron perpendicular velocity is observed, following the same trend as in the experiments.

Note that to further study the evolution of the plasma rotation in presence of RMPs, the physics of the toroidal momentum damping by the neoclassical toroidal viscosity (NTV) should be taken into account. In more or less recent NTV papers and modeling,[48–52] NTV is estimated in MHD codes "*a posteriori*" using analytic solution of drift-kinetic equation for trapped particles at different collisionality regimes. The solution strongly depends both on the perturbed magnetic field which was usually calculated in vacuum, or in approximation of ideal MHD response (no-islands)[49] and on the radial electric field which defines the drift frequency. It should therefore be calculated taking into account the plasma response. However, so far we do not see a good agreement between the modeling using analytical approximate kinetic solution and the experiments. The simple reason for this disagreement is that a consistent computation of the plasma response needs both the kinetic and MHD aspects to self-consistently include the effects of a perturbed magnetic field and of the plasma radial electric field. Such a kinetic-MHD computation is currently beyond the scope of available models and will give rise to forthcoming work.

The present work represents an initial stage of this study. In particular, our present and future works are mainly focused on the interaction of RMPs with ELMs in realistic experimental cases.

ACKNOWLEDGMENTS

This work, supported by the European Communities under the contract of Association between EURATOM and CEA, was carried out within the framework of the European Fusion Development Agreement. The views and opinions expressed herein do not necessarily reflect either those of the European Commission or those of the ITER Organization. This work has benefited from financial support from the National French Research Program (ANR): ANEMOS (2011) and E2T2(2010). The work of Pavel Cahyna was funded by the Grant Agency of the Czech Republic under Grant No. P205/11/2341. Modeling was mainly done on the supercomputers HPC-FF (Julich, Germany), JADE (CINES, France), HELIOS (IFERC, Japan) and CCAMU (Marseille, France). One of the authors (F. Orain) acknowledges Thomas Cartier-Michaud for fruitful discussions.

APPENDIX: LINEARIZATION OF THE OHM's LAW: NON-SCREENING OF THE RMPs WHEN ELECTRON PERPENDICULAR VELOCITY CANCELS

It was found that the cancellation of the perpendicular velocity (A4) on the resonant surfaces implies the vanishing of the screening currents, which is the "no screening" condition for RMPs.[12] This can be shown by linearizing the Ohm's law (9) using the Fourier transform $A(\psi_{0,0},\theta,\varphi) = A_{0,0}(\psi_{0,0}) + A_{m,n}(\psi_{0,0})e^{i(m\theta+n\varphi)}$ of the variables P, ψ, and J. m and n are the poloidal and toroidal mode numbers, respectively, and $\psi_{0,0}$ is the equilibrium poloidal flux (label of the flux surfaces). We consider a single mode (m,n) developing on the resonant surface $q = m/n$. The system is supposed to be at the steady state, which means that the growth of the mode has arrived at saturation. We also suppose that the density perturbation is low compared to the average value: $\rho \sim \rho_{0,0}$. In the framework of our model, we assume that electron and ion temperature are equal but the following calculation remains true if $T_i \neq T_e$. At the first order, Eq. (9) yields

$$0 = \frac{F_0}{R^2} in\left(-u_{m,n} + \frac{\tau_{IC}}{\rho_{0,0}} P_{m,n}\right) + \frac{im}{R}\psi_{m,n}\left(-\partial_\psi u_{0,0} + \frac{\tau_{IC}}{\rho_{0,0}}\partial_\psi P_{0,0}\right) - \frac{im}{R}\nabla\psi_{0,0}\left(-u_{m,n} + \frac{\tau_{IC}}{\rho_{0,0}} P_{m,n}\right) + \frac{\eta}{R^2} J_{m,n}. \tag{A1}$$

Using the definition of the safety factor $q = \frac{\vec{B}\cdot\nabla\varphi}{\vec{B}\cdot\nabla\theta} = \frac{F_0/R^2}{|\nabla\psi|/R} = \frac{F_0}{R|\nabla\psi|}$, Eq. (A1) becomes

$$\frac{iF_0}{R^2}\left(\frac{\tau_{IC}}{\rho_{0,0}} P_{m,n} - u_{m,n}\right)\left(\frac{m}{q} - n\right) + \frac{im}{R}\psi_{m,n}\left(\frac{\tau_{IC}}{\rho_{0,0}}\partial_\psi P_{0,0} - \partial_\psi u_{0,0}\right) = \frac{\eta}{R^2} J_{m,n}. \tag{A2}$$

On the resonant surface, $q = m/n$, which implies

$$\frac{im}{R}\psi_{m,n}\left(\frac{\tau_{IC}}{\rho_{0,0}}\partial_\psi P_{0,0} - \partial_\psi u_{0,0}\right) = \frac{\eta}{R^2} J_{m,n}. \tag{A3}$$

We can write the perpendicular component of the electron velocity

$$\begin{aligned} V_{\perp,e} &= (\vec{V}_e^{\,*} + \vec{V}_{E\times B})\cdot\vec{e}_\theta \\ &= \left(\frac{R^2\tau_{IC}}{\rho}\nabla P\times\nabla\varphi - R^2\nabla u\times\nabla\varphi\right)\cdot\vec{e}_\theta \\ &= R\left(\frac{\tau_{IC}}{\rho}\nabla_\perp P - \nabla_\perp u\right)\cdot\frac{\nabla\psi}{|\nabla\psi|} \\ &= R\left(\frac{\tau_{IC}}{\rho_{0,0}}\partial_\psi P_{0,0} - \partial_\psi u_{0,0}\right). \end{aligned} \tag{A4}$$

The combination of the Eqs. (A4) and (A3) yields

$$imV_{\perp,e}\psi_{m,n} = \eta J_{m,n}. \tag{A5}$$

This relation shows that the current perturbation which appears on the resonant surface $q = m/n$ in response to the magnetic perturbation is proportional to the local electron perpendicular velocity $V_{\perp,e}$. Therefore, it appears that the cancellation of the perpendicular flow on a resonant surface is the non-screening condition of the corresponding RMP harmonics (m,n) by the plasma rotation. The surfaces where this condition is fulfilled can be found via a q_{95}-scan, which shifts the radial position of the resonant surfaces.

[1]R. J. Hawryluk, D. J. Campbell, G. Janeschitz, P. R. Thomas, R. Albanese, R. Ambrosino, C. Bachmann, L. Baylor, M. Bécoulet, I. Benfatto, J. Bialek, A. Boozer, A. Brooks, R. Budny, T. Casper, M. Cavinato, J.-J. Cordier, V. Chuyanov, E. Doyle, T. Evans, G. Federici, M. Fenstermacher, H. Fujieda, K. G'al, A. Garofalo, L. Garzotti, D. Gates, Y. Gribov, P. Heitzenroeder, T. C. Hender, N. Holtkamp, D. Humphreys, I. Hutchinson, K. Ioki, J. Johner, G. Johnson, Y. Kamada, A. Kavin, C. Kessel, R. Khayrutdinov, G. Kramer, A. Kukushkin, K. Lackner, I. Landman, P. Lang, Y. Liang, J. Linke, B. Lipschultz, A. Loarte, G. D. Loesser, C. Lowry, T. Luce, V. Lukash, S. Maruyama, M. Mattei, J. Menard, M. Merola, A. Mineev, N. Mitchell, E. Nardon, R. Nazikian, B. Nelson, C. Neumeyer, J.-K. Park, R. Pearce, R. A. Pitts, A. Polevoi, A. Portone, M. Okabayashi, P. H. Rebut, V. Riccardo, J. Roth, S. Sabbagh, G. Saibene, G. Sannazzaro, M. Schaffer, M. Shimada, A. Sen, A. Sips, C. H. Skinner, P. Snyder, R. Stambaugh, E. Strait, M. Sugihara, E. Tsitrone, J. Urano, M. Valovic, M. Wade, J. Wesley, R. White, D. G. Whyte, S. Wu, M. Wykes, and L. Zakharov, "Principal physics developments evaluated in the ITER design review," Nucl. Fusion **49**(6), 065012 (2009).

[2]M. E. Fenstermacher, T. E. Evans, T. H. Osborne, M. J. Schaffer, M. P. Aldan, J. S. deGrassie, P. Gohil, I. Joseph, R. A. Moyer, P. B. Snyder, R. J. Groebner, M. Jakubowski, A. W. Leonard, O. Schmitz, and DIII-D team, "Effect of island overlap on edge localized mode suppression by resonant magnetic perturbations in DIII-D," Phys. Plasmas **15**, 056122 (2008).

[3]T. E. Evans, M. E. Fenstermacher, R. A. Moyer, T. H. Osborne, J. G. Watkins, P. Gohil, I. Joseph, M. J. Schaffer, L. R. Baylor, M. Bcoulet, J. A. Boedo, K. H. Burrell, J. S. deGrassie, K. H. Finken, T. Jernigan, M. W. Jakubowski, C. J. Lasnier, M. Lehnen, A. W. Leonard, J. Lonnroth, E. Nardon, V. Parail, O. Schmitz, B. Unterberg, and W. P. West, "RMP ELM suppression in DIII-D plasmas with ITER similar shapes and collisionalities," Nucl. Fusion **48**(2), 024002 (2008).

[4]W. Suttrop, T. Eich, J. C. Fuchs, S. Günter, A. Janzer, A. Herrmann, A. Kallenbach, P. T. Lang, T. Lunt, M. Maraschek, R. M. McDermott, A. Mlynek, T. Pütterich, M. Rott, T. Vierle, E. Wolfrum, Q. Yu, I. Zammuto, and H. Zohm, "First observation of edge localized modes mitigation with resonant and nonresonant magnetic perturbations in ASDEX upgrade," Phys. Rev. Lett. **106**, 225004 (2011).

[5]Y. M. Jeon, J.-K. Park, S. W. Yoon, W. H. Ko, S. G. Lee, K. D. Lee, G. S. Yun, Y. U. Nam, W. C. Kim, J.-G. Kwak, K. S. Lee, H. K. Kim, and H. L. Yang, "Suppression of edge localized modes in high-confinement KSTAR

plasmas by nonaxisymmetric magnetic perturbations," Phys. Rev. Lett. **109**, 035004 (2012).
[6]Y. Liang, H. R. Koslowski, P. R. Thomas, E. Nardon, B. Alper, P. Andrew, Y. Andrew, G. Arnoux, Y. Baranov, M. Becoulet, M. Beurskens, T. Biewer, M. Bigi, K. Crombé, E. De La Luna, P. de Vries, W. Fundamenski, S. Gerasimov, C. Giroud, M. P. Gryaznevich, N. Hawkes, S. Hotchin, D. Howell, S. Jachmich, V. Kiptily, L. Moreira, V. Parail, S. D. Pinches, E. Rachlew, and O. Zimmermann, "Active control of type-I edge-localized modes with n = 1 perturbation fields in the jet tokamak," Phys. Rev. Lett. **98**(26), 265004 (2007).
[7]A. Kirk, E. Nardon, R. Akers, M. Bécoulet, G. De Temmerman, B. Dudson, B. Hnat, Y. Q. Liu, R. Martin, P. Tamain, D. Taylor, and the MAST team, "Resonant magnetic perturbation experiments on MAST using external and internal coils for ELM control," Nucl. Fusion **50**(3), 034008 (2010).
[8]J. M. Canik, R. Maingi, T. E. Evans, R. E. Bell, S. P. Gerhardt, H. W. Kugel, B. P. LeBlanc, J. Manickam, J. E. Menard, T. H. Osborne, J.-K. Park, S. Paul, P. B. Snyder, S. A. Sabbagh, E. A. Unterberg, and the NSTX team, "ELM destabilization by externally applied non-axisymmetric magnetic perturbations in NSTX," Nucl. Fusion **50**(3), 034012 (2010).
[9]M. J. Schaffer, J. E. Menard, M. P. Aldan, J. M. Bialek, T. E. Evans, and R. A. Moyer, "Study of in-vessel nonaxisymmetric ELM suppression coil concepts for ITER," Nucl. Fusion **48**(2), 024004 (2008).
[10]H. R. Strauss, L. Sugiyama, G. Y. Park, C. S. Chang, S. Ku, and I. Joseph, "Extended MHD simulation of resonant magnetic perturbations," Nucl. Fusion **49**(5), 055025 (2009).
[11]E. Nardon, P. Tamain, M. Bécoulet, G. Huysmans, and F. L. Waelbroeck, "Quasi-linear MHD modelling of H-mode plasma response to resonant magnetic perturbations," Nucl. Fusion **50**(3), 034002 (2010).
[12]M. Bécoulet, F. Orain, P. Maget, N. Mellet, X. Garbet, E. Nardon, G. T. A. Huysmans, T. Casper, A. Loarte, P. Cahyna, A. Smolyakov, F. L. Waelbroeck, M. Schaffer, T. Evans, Y. Liang, O. Schmitz, M. Beurskens, V. Rozhansky, and E. Kaveeva, "Screening of resonant magnetic perturbations by flows in tokamaks," Nucl. Fusion **52**(5), 054003 (2012).
[13]N. M. Ferraro, "Calculations of two-fluid linear response to non-axisymmetric fields in tokamaks," Phys. Plasmas **19**(5), 056105 (2012).
[14]Y. Liu, A. Kirk, and E. Nardon, "Full toroidal plasma response to externally applied nonaxisymmetric magnetic fields," Phys. Plasmas **17**(12), 122502 (2010).
[15]Q. Yu and S. Guenter, "Plasma response to externally applied resonant magnetic perturbations," Nucl. Fusion **51**, 073030 (2011). Available at http://iopscience.iop.org/0029-5515/51/7/073030.
[16]R. Fitzpatrick, "Bifurcated states of a rotating tokamak plasma in the presence of a static error-field," Phys. Plasmas **5**(9), 3325–3341 (1998).
[17]G. T. A. Huysmans, S. Pamela, E. van der Plas, and P. Ramet, "Non-linear MHD simulations of edge localized modes (ELMS)," Plasma Phys. Controlled Fusion **51**(12), 124012 (2009).
[18]H. R. Strauss, "Reduced MHD in nearly potential magnetic fields," J. Plasma Phys. **57**(Part 1), 83–87 (1997).
[19]R. D. Hazeltine, M. Kotschenreuther, and P. J. Morrison, "A four-field model for tokamak plasma dynamics," Phys. Fluids **28**(8), 2466–2477 (1985).
[20]T. A. Gianakon, S. E. Kruger, and C. C. Hegna, "Heuristic closures for numerical simulations of neoclassical tearing modes," Phys. Plasmas **9**(2), 536–547 (2002).
[21]C. E. Kessel, "Bootstrap current in a tokamak," Nucl. Fusion **34**(9), 1221 (1994).
[22]Y. Sarazin, V. Grandgirard, J. Abiteboul, S. Allfrey, X. Garbet, Ph. Ghendrih, G. Latu, A. Strugarek, and G. Dif-Pradalier, "Large scale dynamics in flux driven gyrokinetic turbulence," Nucl. Fusion **50**(5), 054004 (2010).
[23]M. Bécoulet, E. Nardon, G. Huysmans, W. Zwingmann, P. Thomas, M. Lipa, R. Moyer, T. Evans, V. Chuyanov, Y. Gribov, A. Polevoi, G. Vayakis, G. Federici, G. Saibene, A. Portone, A. Loarte, C. Doebert, C. Gimblett, J. Hastie, and V. Parail, "Numerical study of the resonant magnetic perturbations for type I edge localized modes control in ITER," Nucl. Fusion **48**(2), 024003 (2008).
[24]S. Nishimura, S. Toda, M. Yagi, and Y. Narushima, "Nonlinear stability of magnetic islands in a rotating helical plasma," Phys. Plasmas **19**, 122510 (2012).
[25]Y. Andrew, N. C. Hawkes, T. Biewer, K. Crombe, D. Keeling, E. De La Luna, C. Giroud, A. Korotkov, A. Meigs, A. Murari, I. Nunes, R. Sartori, T. Tala, and JET-EFDA contributors, "Evolution of the radial electric field in a jet H-mode plasma," EPL **83**, 15003 (2008).
[26]F. Orain, M. Bécoulet, G. T. A. Huysmans, G. Dif-Pradalier, V. Grandgirard, G. Latu, P. Maget, N. Mellet, E. Nardon, C. Passeron, and A. Ratnani, "Interaction of resonant magnetic perturbations with flows in toroidal geometry," in 39th European Physical Society Conference on Plasma Physics and 16th International Congress on Plasma Physics Stockholm, Sweden, 2–6 July 2012.
[27]M. Lieberman and A. Lichtenberg, *Regular and Stochastic Motion*, Applied Mathematical Sciences Vol. 38 (Springer, New York, 1983).
[28]V. A. Izzo and I. Joseph, "RMP enhanced transport and rotational screening in simulations of DIII-D plasmas," Nucl. Fusion **48**, 115004 (2008).
[29]R. A. Moyer, T. E. Evans, T. H. Osborne, P. R. Thomas, M. Bécoulet, J. Harris, K. H. Finken, J. A. Boedo, E. J. Doyle, M. E. Fenstermacher, P. Gohil, R. J. Groebner, M. Groth, G. L. Jackson, R. J. La Haye, C. J. Lasnier, A. W. Leonard, G. R. McKee, H. Reimerdes, T. L. Rhodes, D. L. Rudakov, M. J. Schaffer, P. B. Snyder, M. R. Wade, G. Wang, J. G. Watkins, W. P. West, and L. Zeng, "Edge localized mode control with an edge resonant magnetic perturbation," Phys. Plasmas **12**, 056119 (2005).
[30]M. F. Heyn, I. B. Ivanov, S. V. Kasilov, W. Kernbichler, I. Joseph, R. A. Moyer, and A. M. Runov, "Kinetic estimate of the shielding of resonant magnetic field perturbations by the plasma in DIII-D," Nucl. Fusion **48**(2), 024005 (2008).
[31]F. L. Waelbroeck, I. Joseph, E. Nardon, M. Bécoulet, and R. Fitzpatrick, "Role of singular layers in the plasma response to resonant magnetic perturbations," Nucl. Fusion **52**(7), 074004 (2012).
[32]Y. Liu, M. S. Chu, Y. In, and M. Okabayashi, "Resonant field amplification with feedback-stabilized regime in current driven resistive wall mode," Phys. Plasmas **17**, 072510 (2010).
[33]I. Joseph, T. E. Evans, A. M. Runov, M. E. Fenstermacher, M. Groth, S. V. Kasilov, C. J. Lasnier, R. A. Moyer, G. D. Porter, M. J. Schaffer, R. Schneider, and J. G. Watkins, "Calculation of stochastic thermal transport due to resonant magnetic perturbations in DIII-D," Nucl. Fusion **48**(4), 045009 (2008).
[34]T. E. Evans, R. K. W. Roeder, J. A. Carter, B. I. Rapoport, M. E. Fenstermacher, and C. J. Lasnier, "Experimental signatures of homoclinic tangles in poloidally diverted tokamaks," J. Phys.: Conf. Ser. **7**, 174–190 (2005).
[35]A. Kirk, J. Harrison, Y. Liu, E. Nardon, I. T. Chapman, and P. Denner, "Observation of lobes near the *x* point in resonant magnetic perturbation experiments on MAST," Phys. Rev. Lett. **108**, 255003 (2012).
[36]I. T. Chapman, A. Kirk, S. Saarelma, J. R. Harrison, R. Scannell, and MAST team, "Towards understanding elm mitigation: The effect of axisymmetric lobe structures near the x-point on elm stability," Nucl. Fusion **52**, 123006 (2012).
[37]P. Cahyna, M. Peterka, A. Kirk, A. Thornton, J. Harrison, D. Muir, and R. Panek, "Strike point splitting induced by the application of magnetic perturbations on MAST," J. Nucl. Mater. **438** (Suppl.) S326–S329 (2013).
[38]T. E. Evans, I. Joseph, R. A. Moyer, M. E. Fenstermacher, C. J. Lasnier, and L. W. Yan, "Experimental and numerical studies of separatrix splitting and magnetic footprints in DIII-D," J. Nucl. Mater. **363–365**, 570–574 (2007).
[39]O. Schmitz, T. E. Evans, M. E. Fenstermacher, H. Frerichs, M. W. Jakubowski, M. J. Schaffer, A. Wingen, W. P. West, N. H. Brooks, K. H. Burrell, J. S. deGrassie, Y. Feng, K. H. Finken, P. Gohil, M. Groth, I. Joseph, C. J. Lasnier, M. Lehnen, A. W. Leonard, S. Mordijck, R. A. Moyer, A. Nicolai, T. H. Osborne, D. Reiter, U. Samm, K. H. Spatschek, H. Stoschus, B. Unterberg, E. A. Unterberg, J. G. Watkins, R. Wolf, and the DIII-D and TEXTOR teams, "Aspects of three dimensional transport for ELM control experiments in ITER-similar shape plasmas at low collisionality in DIII-D," Plasma Phys. Controlled Fusion **50**(12), 124029 (2008).
[40]E. Nardon, P. Cahyna, S. Devaux, A. Kirk, A. Alfier, E. De La Luna, G. de Temmerman, P. Denner, T. Eich, T. Gerbaud, D. Harting, S. Jachmich, H. R. Koslowski, Y. Liang, and Y. Sun, "Strike-point splitting induced by external magnetic perturbations: Observations on JET and MAST and associated modelling," J. Nucl. Mater. **415**(1, Supplement), S914–S917 (2011).
[41]P. Cahyna, E. Nardon, and JET EFDA contributors, "Model for screening of resonant magnetic perturbations by plasma in a realistic tokamak geometry and its impact on divertor strike points," J. Nucl. Mater. **415**(1, Supplement), S927–S931 (2011).
[42]P. Cahyna, Y. Q. Liu, E. Nardon, A. Kirk, M. Peterka, J. R. Harrison, A. Thornton, I. Chapman, R. Panek, O. Schmitz, and the MAST team, "Modelling of plasma response to resonant magnetic perturbations and its influence on divertor strike points," in *Proceedings of 24th IAEA Fusion Energy Conference (FEC), San Diego, 2012* (IAEA, Vienna, 2013), p. TH/P4-27.
[43]O. Schmitz, M. Becoulet, P. Cahyna, T. E. Evans, Y. Feng, H. Frerichs, A. Kischner, A. Kukushkin, R. Laengner, T. Lunt, A. Loarte, R. Pitts, D. Reiser, D. Reiter, G. Saibene, and U. Samm, "Modeling of divertor particle and heat loads during application of resonant magnetic perturbation fields for ELM control in ITER," J. Nucl. Mater. **438** (Suppl.), S194–S198 (2013).

[44]H. Frerichs, D. Reiter, O. Schmitz, P. Cahyna, T. E. Evans, Y. Feng, and E. Nardon, "Impact of screening of resonant magnetic perturbations in three dimensional edge plasma transport simulations for DIII-D," Phys. Plasmas **19**(5), 052507 (2012).
[45]S. J. P. Pamela, G. T. A. Huijsmans, A. Kirk, I. T. Chapman, J. R. Harrison, R. Scannell, A. J. Thornton, M. Becoulet, and F. Orain, "Resistive MHD simulation of edge-localized-modes for double-null discharges in the mast device," Plasma Phys. Controlled Fusion **55**, 095001 (2013).
[46]A. Kirk, Y. Liu, E. Nardon, P. Tamain, P. Cahyna, I. Chapman, P. Denner, H. Meyer, S. Mordijck, D. Temple, and MAST team, "Magnetic perturbation experiments on MAST L- and H-mode plasmas using internal coils," Plasma Phys. Controlled Fusion **53**, 065011 (2011).
[47]A. Kirk, I. T. Chapman, J. Harrison, Y. Liu, E. Nardon, S. Saarelma, R. Scannell, A. J. Thornton, and MAST team, "Effect of resonant magnetic perturbations with toroidal mode numbers of 4 and 6 on edge-localized modes in single null H-mode plasmas in MAST," Plasma Phys. Controlled Fusion **55**, 015006 (2013).
[48]A. J. Cole, C. C. Hegna, and J. D. Callen, "Neoclassical toroidal viscosity and error-field penetration in tokamaks," Phys. Plasmas **15**(5), 056102 (2008).
[49]J.-k. Park, A. H. Boozer, and J. E. Menard, "Nonambipolar transport by trapped particles in tokamaks," Phys. Rev. Lett. **102**, 065002 (2009).
[50]Y. Sun, Y. Liang, K. C. Shaing, H. R. Koslowski, C. Wiegmann, and T. Zhang, "Neoclassical toroidal plasma viscosity torque in collisionless regimes in tokamaks," Phys. Rev. Lett. **105**, 145002 (2010).
[51]M. Becoulet, G. Huysmans, X. Garbet, E. Nardon, D. Howell, A. Garofalo, M. Schaffer, T. Evans, K. Shaing, A. Cole, J. K. Park, and P. Cahyna, "Physics of penetration of resonant magnetic perturbations used for type I edge localized modes suppression in tokamaks," Nucl. Fusion **49**, 085011 (2009).
[52]Y. Q. Liu, A. Kirk, Y. Sun, P. Cahyna, I. T. Chapman, P. Denner, G. Fishpool, A. M. Garofalo, J. R. Harrison, E. Nardon, and the MAST team, "Toroidal modeling of plasma response and resonant magnetic perturbation field penetration," Plasma Phys. Controlled Fusion **54**(12), 124013 (2012).